



1 **Effects of Marine Organic Aerosols as Sources of**
2 **Immersion-Mode Ice Nucleating Particles on High Latitude**
3 **Mixed-Phase Clouds**

4 Xi Zhao¹, Xiaohong Liu¹, Susannah Burrows², and Yang Shi¹,

5 ¹Department of Atmospheric Sciences, Texas A&M University, College Station, Texas, 77840, USA

6 ²Pacific Northwest National Laboratory, Richland, Washington, 99352, USA

7

8

9 *Correspondence to:* Xiaohong Liu (xiaohong.liu@tamu.edu)

10

11



12 **Abstract.** Mixed-phase clouds are frequently observed in the Arctic, Antarctic, and over
13 the Southern Ocean, and have important impacts on the surface energy budget and
14 regional climate. Marine organic aerosol (MOA), a natural source of aerosol emitted over
15 ~70% of Earth's surface, may significantly modify the properties and radiative forcing of
16 mixed-phase clouds. However, the relative importance of MOA as a source of ice
17 nucleating particles (INPs) in comparison to mineral dust, and its effects as cloud
18 condensation nuclei (CCN) and INPs on mixed-phase clouds are still open questions. In
19 this study, we implement MOA as a new aerosol species into the Community
20 Atmosphere Model version 6 (CAM6), the atmosphere component of the Community
21 Earth System Model version 2 (CESM2), and allow the treatments of aerosol-cloud
22 interactions of MOA via droplet activation and ice nucleation. CAM6 reproduces
23 observed seasonal cycles of marine organic matter at Mace Head and Amsterdam Island
24 when the MOA fraction of sea spray aerosol in the model is assumed to depend on sea
25 spray biology, but fails when this fraction is assumed to be constant. Model results
26 indicate that marine INPs dominate primary ice nucleation below 400 hPa over the
27 Southern Ocean and Arctic boundary layer, while dust INPs are more abundant elsewhere.
28 By acting as CCN, MOA exerts a shortwave cloud forcing change of -2.78 W m^{-2} over
29 the Southern Ocean in the austral summer. By acting as INPs, MOA enhances the
30 longwave cloud forcing by 0.35 W m^{-2} over the Southern Ocean in the austral winter.
31 The annual global mean net cloud forcing changes due to CCN and INPs of MOA are
32 -0.35 and 0.016 W m^{-2} , respectively. These findings highlight the vital importance of
33 Earth System Models to consider the MOA as an important aerosol species for the
34 interactions of biogeochemistry, hydrological cycle, and climate change.

35

36

37



38 **1 Introduction**

39 Ice crystals in clouds play a critical role in determining cloud phase, lifetime,
40 electrification, and radiative properties. As a result, cloud ice influences precipitation and
41 cloud radiative forcing. To quantify the impact of ice crystals on the hydrologic cycle and
42 energy budget of the Earth system, it is important to advance the process-based
43 understanding of initiation and evolution of ice particles. Ice particles can be initialized
44 by homogeneous freezing or by heterogeneous nucleation. Homogeneous freezing of
45 cloud droplets and aerosol solution droplets happens when air temperature is below
46 approximately -38°C . In mixed-phase clouds in which air temperature is between -38°C
47 to 0°C , ice is initialized only by heterogeneous nucleation on ice nucleating particles
48 (INPs) (Kanji et al., 2017).

49 INPs have different characteristics in their compositions and origins. Previous
50 studies (Hoose and Möhler, 2012; Murray et al., 2012; Kanji et al., 2017) have shown
51 that mineral dust, primary bioaerosols (e.g., fungal spores, bacteria, and pollen), and
52 volcanic ash can be effective INPs. However, large uncertainties exist surrounding the ice
53 nucleating properties of black carbon and organic carbon from biomass burning and fossil
54 fuel combustion. A majority of INPs are of terrestrial origin. Due to their large emission
55 quantities and high efficiency at forming ice, mineral dust may play a dominant role in
56 ice formation over continents. However, in remote oceanic regions where terrestrial INPs
57 are rare, the aerosol species contributing to INPs and the mechanisms for ice initialization
58 remain poorly understood. Recent observational and modelling studies have shown that
59 marine organic aerosol (MOA) is potentially an important source of INPs over remote
60 oceanic regions (Wilson et al., 2015; DeMott et al., 2016; Vergara-Temprado et al., 2017;
61 Huang et al., 2018; McCluskey et al., 2019).

62 MOA can be generated from both primary and secondary processes during ocean
63 biological activities, producing either water-soluble or insoluble organic aerosols.
64 Previous studies have inferred that water-insoluble marine organic matter is mainly
65 derived from the primary emissions of sea spray aerosols (SSAs) (Ceburnis et al., 2008).
66 In this production process, SSAs and associated organic matter are injected into the marine
67 boundary layer when bubbles burst at the air-sea interface. Long-term measurements of
68 seasonal variability in SSAs (O'Dowd et al., 2004; Yoon et al., 2007; Rinaldi et al., 2013)



69 and organic matter in remote marine air (Sciare et al., 2009) are consistent with the
70 hypothesis that the amount of organic matter is associated with ocean biological activity.
71 Laboratory experiments have also demonstrated that the presence of phytoplankton blooms
72 can be associated with significant changes in the number flux and size distribution of
73 emitted SSAs (Alpert et al., 2015; Rastelli et al., 2017; Forestieri et al., 2018; Christiansen
74 et al., 2019), as well as the SSA organic content (Facchini et al., 2008; Ault et al., 2013).

75 Parameterizations for the primary emission of MOA have been developed with the
76 intention to be used in models. Most of these parameterizations relate MOA emission flux
77 to ocean chlorophyll a concentration [Chl-a]. An advantage of this approach is that [Chl-a]
78 is globally available from satellite-based measurements, especially over the remote oceans
79 where ground-based observations are difficult to conduct. Although [Chl-a] makes up only
80 a minor fraction of the organic matter in the ocean (Gardner et al., 2006), it has a long
81 history as a widely-used proxy for the biomass of phytoplankton in ocean surface waters
82 (Steele et al., 1962; Cullen et al., 1982), and has been used to derive empirical relationships
83 between satellite-observed [Chl-a] and the observed MOA contribution to submicron SSAs.
84 Several studies have also found that measured organic matter in SSA correlates more
85 strongly with ocean [Chl-a] than with other satellite-retrieved ocean chemistry variables,
86 such as particulate organic carbon, dissolved organic carbon, and colored dissolved and
87 detrital organic matter (O'Dowd et al., 2004; Sciare et al., 2009; Gantt et al., 2011; Rinaldi
88 et al., 2013).

89 O'Dowd et al. (2008) proposed a MOA emission parameterization, which was further
90 modified by Langmann et al. (2008) and Vignati et al. (2010). In this parameterization, the
91 fraction of emitted organic matter in SSA has a linear relationship with ocean [Chl-a] and is
92 not dependent on surface wind speed. Gantt et al. (2011) took a step further, and developed
93 an emission parameterization in which the organic matter fraction is an empirical function
94 of ocean [Chl-a], 10 m wind speed, and aerosol size. Both parameterizations from Gantt et
95 al. (2011) and Vignati et al. (2010) were found to capture the magnitude of MOA
96 concentrations compared to observations, but the parameterization from Gantt et al. (2011)
97 had a better representation of seasonal variability of MOA concentrations at Amsterdam
98 Island and Mace Head, Ireland (Meskhidze et al., 2011). Rinaldi et al. (2013) also
99 developed a MOA emission parameterization which depends on surface wind speed and



100 [Chl-a], and by assuming an 8–10 day time lag between upwind ocean [Chl-a] and
101 enhanced production of MOA the correlation between enriched MOA and [Chl-a] was
102 improved. Burrows et al. (2014) proposed a physically-based approach to represent MOA
103 emission process (i.e., OCEANFILMS) instead of using the empirical [Chl-a]. This
104 method was implemented in the DOE Energy Exascale Earth System Model version 1
105 (E3SMv1) (Golaz et al., 2019; Rasch et al., 2019), and the CCN effect of MOA on cloud
106 droplet activation was investigated (Burrows et al., 2018).

107 Recent observational evidence continuously shows the importance of MOA as INPs
108 in natural clouds (Wilson et al., 2015; DeMott et al., 2016; McCluskey et al., 2018a, b).
109 However, there have been very limited modeling studies to quantify the effects of MOA
110 INPs on clouds. Yun and Penner (2013) conducted the first global study of MOA on ice
111 formation and radiative forcing using the CAM3 model. Their study indicated that MOA
112 INPs are the dominant INPs for mixed-phase clouds over the Southern Hemisphere (SH),
113 and after including MOA INPs, the model generated a more reasonable ice water path
114 (IWP) compared with the International Satellite Cloud Climatology Project (ISCCP)
115 observation data. In their study, the model simulated frozen fraction of MOA at -15°C is
116 3.75% for their lowest size bin ($0.05 - 0.63 \mu\text{m}$) and 100% for their larger size bins. These
117 values may be too high compared with both historical and recent measurements of the ice
118 nucleation efficiency of sea surface material (Schnell and Vali, 1975; Wilson et al., 2015)
119 and SSAs (DeMott et al., 2016; McCluskey et al., 2018b).

120 With more measurements of MOA and sea spray INPs becoming available, recent
121 modeling studies have been able to improve upon past MOA INP parameterizations.
122 Huang et al. (2018) used the ECHAM6-HAM2 model to study the MOA influence on ice
123 formation and climate. They followed the [Chl-a]-based of Rinaldi et al. (2013) to
124 represent the MOA emission and compared two empirical methods for calculating the
125 MOA INP efficiency (Wilson et al., 2015; DeMott et al., 2016). They found that MOA
126 influenced the cloud ice number concentration and effective radius only slightly, and MOA
127 did not exert a significant influence on the global radiative balance due to compensating
128 cloud responses. However, these conclusions also depend on the sensitivity of their model
129 to the change in INP number concentration.



130 In contrast to the findings of Huang et al. (2018), Vergara-Temprado et al. (2017) and
131 McCluskey et al. (2019) found that MOA was the dominant source of INPs over the
132 Southern Ocean. Vergara-Temprado et al. (2017) used the Global Model of Aerosol
133 Processes (GLOMAP) to investigate the relative importance of feldspar and MOA for ice
134 nucleation. Ice nucleation by MOA follows the Wilson et al. (2015) parameterization. This
135 study also found that on 10–30 % of days in the study period there were more MOA INPs
136 than feldspar INPs over the Northern Hemisphere (NH) Ocean. McCluskey et al. (2019)
137 used the aerosol concentrations calculated offline from the Community Atmosphere Model
138 version 5 (CAM5) to show that MOA is the dominant INPs over the Southern Ocean. Ice
139 nucleation by MOA follows the McCluskey et al. (2018b) parameterization.

140 Isolating the INP effect of MOA on clouds and radiative forcing has rarely been
141 examined directly, which motivates our study to address MOA ice nucleation process and
142 to better understand the climate influence of MOA INPs. Our approach is different from
143 previous studies. For example, we use a more physically-based approach (Burrows et al.,
144 2014) to represent MOA emission instead of the empirical [Chl-a] based method used in
145 Huang et al. (2018). Instead of the offline evaluation of INP parameterizations in CAM5
146 (McCluskey et al., 2019), this study implements the MOA emission and other process
147 representations in the Community Atmosphere Model version 6 (CAM6), the latest
148 atmosphere component of Community Earth System Model version 2 (CESM2), and
149 allows for the impacts of MOA on modeled clouds and radiative forcing interactively.
150 Lastly, we isolate the INP effect from the CCN effect of MOA in order to better understand
151 the MOA influence on clouds via these two mechanisms.

152 This paper is organized as follows. Section 2 presents the model, parameterizations of
153 MOA as well as model experiments. Section 3 describes the model results and comparison
154 with observations. Section 4 discusses the remaining questions. Section 5 summarizes and
155 draws the conclusions of this study.



156 **2 Methods**

157 **2.1 Model and parameterizations**

158 CAM6 with the Finite-Volume (FV) dynamical core (Lin and Rood, 1997) is used
159 in this study. CAM6 treats important physical processes in the atmosphere, including
160 radiative transfer, deep convection, cloud macrophysics, cloud microphysics, shallow
161 convection, and planetary boundary layer turbulence. Cloud and aerosol interactions with
162 longwave and shortwave radiation transfer are treated by the Rapid Radiative Transfer
163 Model for GCMs (RRTMG) scheme (Iacono et al., 2008; Mlawer et al., 1997). A
164 double-moment scheme (Gettelman et al., 2015) is used to describe the microphysical
165 processes of cloud and precipitation hydrometeors in large-scale stratiform clouds, while
166 the deep convection is represented by the Zhang and McFarlane (1995) scheme. CAM6
167 uses the Cloud Layers Unified By Binormals (CLUBB) scheme (Golaz et al., 2002;
168 Larson et al., 2002) to unify the representations of cloud macrophysics, turbulence, and
169 shallow convection.

170 The four-mode version of the Modal Aerosol Module (MAM4), which is an
171 extension of the three-mode version of MAM (Liu et al., 2012), is used to describe the
172 aerosol properties and processes in CAM6 (Liu et al., 2016). MAM4 uses the modal
173 method to represent the size distributions of four aerosol modes: Aitken, accumulation,
174 coarse, and primary carbon. The original MAM4 encompasses six aerosol species: black
175 carbon, dust, primary organic aerosol, sea salt, secondary organic aerosol, and sulfate
176 (Table 1). The primary organic aerosol here refers to non-marine sources of organic
177 matter, usually from terrestrial biomass burning, fossil fuel, and biofuel burning. Aerosol
178 species are internally-mixed within a mode and externally-mixed between modes. The
179 mass mixing ratio of each aerosol species within a mode and the total number mixing
180 ratio of aerosols in that mode are predicted in the model. Then the log-normal size
181 distribution can be determined for each mode based on a prescribed geometric standard
182 deviation (Table 1). Different aerosol species are characterized by a variety of properties
183 such as hygroscopicity, density, and optical properties (Table 2).

184 While anthropogenic aerosol and precursor gas emissions are prescribed for
185 model simulations, emissions of natural aerosols (e.g., SSA, dust) are calculated



186 interactively in the model. SSA in MAM is emitted following the parameterization of
187 Mårtensson et al. (2003) for dry particle diameters from 0.020 to 2.8 μm , and Monahan et
188 al. (1986) from 2.8 to 10 μm . The Mårtensson et al. parameterization is derived from
189 laboratory experiments in which particles were produced by bubble bursting using a
190 sintered glass filter in synthetic seawater. The emission rate depends linearly on the sea
191 surface temperature and is proportional to 10-m wind speed, raised to the power of 3.41
192 (Monahan et al., 1986; Gong et al., 1997).

193

194 2.2 MOA in CAM6

195 In this study, several modifications are implemented in CAM6 in order to
196 explicitly quantify the influence of marine organic matter on aerosols, clouds, and
197 radiation. These modifications are comprised of (1) emission schemes of MOA, as
198 introduced in section 2.2.1, and (2) ice nucleation parameterizations for MOA, as
199 introduced in section 2.2.2.

200 2.2.1 Emission of MOA

201 Three different methods for online MOA emissions are implemented in CAM6.
202 These methods parameterize the organic mass fraction of sea spray and use the fraction to
203 compute MOA emissions based on the emission rate of SSA.

204 The mass fraction of MOA in total SSA, $F_{MOA/SSA}$ is defined as the following:

$$205 F_{MOA/SSA} = \frac{M_{MOA}}{M_{sea\ spray}} = \frac{M_{MOA}}{M_{MOA} + M_{sea\ salt}} \quad (1)$$

206 in which M_{MOA} is the mass mixing ratio of MOA, and $M_{sea\ salt}$ is the mass mixing
207 ratio of sea salt. Thus, the emitted MOA mass mixing ratio can be computed as:

$$208 M_{MOA} = \frac{F_{MOA/SSA} \times M_{sea\ salt}}{1 - F_{MOA/SSA}} \quad (2)$$

209 The emitted MOA number mixing ratio is calculated based on the emitted mass
210 mixing ratio and particle density of MOA, the latter of which is set to be 1601 kg m^{-3}
211 (Liu et al., 2012), as given in Table 2.

212 Differences between the three emission methods lie in how to determine the
213 organic mass fraction $F_{MOA/SSA}$. These methods are compared in this study: the first is



214 the Langmuir isotherm-based parameterization by Burrows et al. (2014) (B14), the
215 second is based on wind speed and [Chl-a] by Gantt et al. (2011) (G11), and the third,
216 which represents a null hypothesis, assumes a fixed mass fraction between organic matter
217 and sea salt (NULL).

218 a. G11 emission scheme

219 A chlorophyll-based emission scheme of MOA was derived based on the [Chl-a]
220 and the 10-m wind speed (Gantt et al. (2011), hereafter referred to as G11). In this
221 method, the organic mass fraction of sea spray is parameterized as:

$$222 \quad F_{MOA/SSA} = \frac{\frac{1}{1+0.03 \times e^{6.81 \times D_p}} + 0.03}{1 + e^{-2.63 \times (Chl-a) + 0.18 U_{10}}} \quad (3)$$

223 where D_p is the dry diameter of particles.

224 b. B14 emission scheme

225 Different from the earlier empirical chlorophyll-based scheme, a physically-based
226 scheme, named OCEANFILMS was proposed for modeling the relationship between
227 emitted SSA chemistry and ocean biogeochemistry (Burrows et al. (2014), hereafter
228 referred to as B14). The Langmuir isotherm-based mechanism is adopted to describe the
229 organic enrichment on the bubble film. When the bubble film bursts, the film breaks up
230 into film drops, which are suspended in the air. After evaporation of water from these
231 droplets, the remaining suspending materials form MOA and sea salt aerosol particles. In
232 this method, the organic matter on one side of the bubble film (per area) is determined
233 by:

$$234 \quad M_{s_MOA} = S_m \times \theta \quad (4)$$

235 where S_m is the organic mass per area at saturation (Table 3), and θ is the surface
236 coverage fraction of organics calculated based on the Langmuir adsorption equilibrium
237 assumption:

$$238 \quad \theta = \frac{\alpha \times C_M}{1 + \alpha \times C_M} \quad (5)$$

239 where α is the Langmuir parameter as prescribed in Table 3, and C_M is the mass
240 concentration of organic matters in the ocean. C_M is prescribed from the monthly mean
241 surface distribution of macromolecule concentrations, which is generated by ocean



242 biogeochemical simulations (Burrows et al., 2014). In this method, three different organic
243 classes are considered with molecular weights and mass per area at saturation as
244 prescribed in Table 3.

245 Based on Equations (1), (4), and (5), the organic mass fraction of sea spray is
246 expressed as:

$$247 \quad F_{MOA/SSA} = \frac{S_m \times \frac{\alpha \times C_M}{1 + \alpha \times C_M}}{S_m \times \frac{\alpha \times C_M}{1 + \alpha \times C_M} + M_{s_sea\ salt}} \quad (6)$$

248 $M_{s_sea\ salt}$ is the sea salt mass per area of bubble surface, which is set to be 0.0035875 g
249 m^{-2} .

250

251 c. NULL emission hypothesis

252 Null hypothesis assumes that the organic mass fraction of SSA is constant, and
253 does not vary geographically or seasonally. If we are to adopt a parameterization for the
254 seasonal dependence of MOA, it is desirable to demonstrate that the agreement with
255 observations of MOA is improved by such a parameterization, compared with the null
256 hypothesis that no such relationship exists. The choice of the “null” hypothesis is
257 motivated in part by Quinn et al. (2014) and Bates et al. (2020), who measured roughly
258 constant values of $F_{MOA/SSA}$ in SSAs generated at sea by using a floating device to
259 generate and sample spray, during five sea-going ship campaigns. These studies
260 measured $F_{MOA/SSA}$ values of roughly 0.7–0.9 in sub-0.180 μm particles, and roughly
261 0.05–0.3 in sub-1.1 μm particles.

262 Loosely following the results of Quinn et al. (2014) and Bates et al. (2020), we set
263 $F_{MOA/SSA}$ to 0.8 in the Aitken mode, and to 0.05 in the accumulation mode (see Table 1
264 for the size ranges of Aitken and accumulation modes). For comparison, Facchini et al.
265 (2008) measured SSA generated from oceanic water for its organic and salt content, and
266 found that organic matter comprised roughly 75% of particles in the size range
267 0.125–0.250 μm , and that this fraction decreased with increasing particle size to about 5%
268 of 1 μm particles. Similarly, Prather et al. (2013) analyzed sea spray generated in a wave
269 tank during a mesocosm bloom experiment and reported that about 80% of 0.080 μm
270 particles were classified as organic carbon by transmission electron microscopy (TEM)



271 with energy-dispersive X-ray (EDX), while a few percents of 1 μm particles were
272 classified as either organic carbon or biological species by the aerosol TOF mass
273 spectrometry (ATOFMS).

274

275 **2.2.2 Effects of MOA on clouds as CCN and INPs**

276 MOA is emitted into different aerosol modes depending on mixing state of MOA
277 and sea salt (Burrows et al., 2014, 2018). In the internally-mixed emission approach,
278 MOA is emitted into the accumulation and Aitken modes along with sea salt, as shown in
279 Table 1. In contrast, MOA is emitted into the accumulation and primary carbon modes in
280 the externally-mixed emission approach. Furthermore, the emission of MOA can replace
281 or be added to sea salt emission in terms of mass and number in the model. Burrows et al.
282 (2018) found that simulated MOA amounts, seasonal cycles, and impacts on CCN over
283 the Southern Ocean show better agreement with observations under the assumption that
284 emitted MOA is added to, and internally mixed with, sea salt. As shown in Table 2, the
285 hygroscopicity of MOA is set to be 0.1 following Burrows et al. (2014, 2018), compared
286 to 1.16 for sea salt. The mode hygroscopicity is calculated as the volume-weighted
287 average of all species in a mode, which is then used in the Abdul-Razzak and Ghan (2000)
288 droplet activation parameterization in CAM6.

289 In this study, in addition to the CCN effect of MOA, we also include its effect on
290 clouds as INPs. For this purpose, two different ice nucleation parameterizations for MOA
291 are implemented in CAM6. Additionally, we examine the relative importance of MOA to
292 dust INPs with different ice nucleation parameterizations.

293 **a. W15 ice nucleation scheme of MOA**

294 An INP parameterization for MOA was proposed based on immersion-freezing
295 measurements of materials aerosolized from sea surface microlayer (SML) water samples
296 collected in the North Atlantic and Arctic Oceans (Wilson et al., 2015). In this
297 parameterization (hereafter as W15), the number concentration of MOA INPs is a
298 function of temperature (T) and the total organic carbon (TOC) mass concentration, given
299 as:

300



301
$$N_{IN,T} = TOC \times e^{(11.2186 - (0.4459 \times T))} \quad (7)$$

302

303 W15 assumes that relationship between TOC and INPs in airborne sea spray is the
304 same as that in SML samples due to limited measurement data in the early stage.
305 However, recent research suggests that INPs may be transferred differently from TOC
306 during the sea spray production (Wang et al., 2017), calling this assumption into question.
307 The quantitative importance of this selective transfer of INPs from SML to the SSAs is a
308 topic requiring further research beyond the scope of the current study and is not
309 accounted for here. Additionally, this approach did not attempt to correct for the possible
310 entrainment of multiple ice-nucleating entities into a single sea spray particle.

311 **b. M18 ice nucleation scheme of MOA**

312 Another empirical INP parameterization of MOA was derived based on the
313 correlation between ambient aerosols and INPs measured during the “clean scenario” at
314 Mace Head Station in August 2015 (McCluskey et al., 2018a, hereafter as M18).
315 Therefore, M18 includes the effect of physiochemical selective emission and aerosol
316 chemistry in the air which is missed in W15. This parameterization follows the same
317 functional form as the surface-active site density (n_s) parameterization of Niemand et al.
318 (2012) for dust, but with different coefficients for MOA, as given below:

319
$$n_s(T) = e^{(-0.545(T-273.15)+1.0125)} \quad (8)$$

320 **c. N12 ice nucleation scheme of dust**

321 A surface-active site density-based ice nucleation scheme for immersion freezing
322 on dust was derived by Niemand et al. (2012) (hereafter referred to as N12) based on
323 measurements of the AIDA cloud chamber. N12 relates the number concentration of dust
324 INPs to the dust aerosol number concentration (N_{tot}), dust particle surface area (S_{ae} ,
325 calculated based on dry diameter of particles), and the density of ice-active surface sites
326 at a given temperature T ($n_s(T)$), shown as:

327

328
$$N_{INP}(T) = N_{tot} S_{ae} n_s(T) \quad (9)$$

329 in which $n_s(T)$ is given as:



330
$$n_s(T) = e^{(-0.517(T-273.15)+8.934)} \quad (10)$$

331 N12 is valid in the temperature range from -36 to -12 °C.

332

333 **d. D15 ice nucleation scheme of dust**

334 As the N12 scheme relates INPs to all sizes of dust aerosol, it may overestimate
335 INPs, since smaller dust aerosol (<0.5 μm) may not be effective as INPs. An empirical
336 ice nucleation scheme for the immersion freezing on dust aerosol with sizes larger than
337 0.5 μm was derived based on field and laboratory measurements (DeMott et al., 2015)
338 (hereafter referred to as D15). The dust INP number concentration is calculated as

339

340
$$N_{INP}(T) = a(n_{0.5})^b e^{c(T-273.15)-d} \quad (11)$$

341

342 where $a = 3$, $b = 1.25$, $c = -0.46$, $d = 11.6$, and $n_{0.5}$ is the number concentration of dust
343 particles with diameters larger than 0.5 μm .

344 We note that the above ice nucleation parameterizations (W15, M18, N12, and
345 D15) are based on empirical formulations. The default heterogeneous ice nucleation
346 parameterization in CAM6 follows the classical nucleation theory (CNT) (Wang et al.,
347 2014). CNT is a stochastic scheme that links the freezing rate to the number
348 concentrations of dust and black carbon aerosols through different heterogeneous ice
349 nucleation mechanisms (deposition, contact, and immersion). Due to large uncertainties
350 in heterogeneous nucleation parameterizations, we conducted several ice nucleation
351 sensitivity experiments in CAM6 as will be discussed in section 2.3.

352 **2.3 Model configurations and experiments**

353 In this study, we carried out several numerical experiments to investigate the
354 influence of MOA on aerosols as well as CCN and INP activities (Table 4). All
355 simulations were performed for 10 years with prescribed climatological sea surface
356 temperatures and sea ice. The first year of simulations was treated as model spin-up, and
357 last nine years of simulations were used in analyses. The simulations were driven by the
358 present-day (year 2000) aerosol and precursor gas emissions with given greenhouse gas



359 concentrations. The model was run for 32 vertical levels from surface up to 3 hPa with a
360 horizontal resolution of 0.9° (latitudes) by 1.25° (longitude). We conducted two sets of
361 experiments. The first set of experiments, as listed in Table 4, are used to test the model
362 sensitivity to different MOA emission schemes. The baseline experiment (BASE) uses
363 the default CAM6 model which does not account for MOA emission and related physical
364 processes. In addition to the BASE experiment, the B14 experiment addresses emission,
365 advection, dry/wet deposition, and CCN effect of MOA using the Burrows et al. (2014)
366 emission scheme. We also designed two additional experiments (G11 and NULL) to
367 address the model sensitivity to emission methods. These simulations (B14 and G11)
368 were conducted with the added and internally-mixed MOA approach, following Burrows
369 et al. (2018). The INP effect of MOA is not considered in this set of experiments.

370 We conducted another set of experiments to investigate both CCN and INP effects
371 of MOA, as listed in Table 4. The control experiment (CTL) is the same as BASE except
372 that the D15 dust ice nucleation scheme was used to replace the CNT scheme in BASE,
373 because D15 gave a better model performance compared with observations in our
374 previous study (Shi and Liu, 2019). The B14_D15, which is based on CTL, considers the
375 MOA emission from B14 and the CCN effect of MOA. The B14_D15_M18 experiment,
376 which is based on B14_D15, additionally considers the INP effect of MOA based on
377 M18. The comparison between CTL and B14_D15 shows the CCN effect of MOA, while
378 the comparison between B14_D15 and B14_D15_M18 shows its INP effect.

379 We further conducted three experiments to examine the model sensitivity to a
380 different MOA ice nucleation parameterization (i.e., W15) in B14_D15_W15, and to two
381 different dust ice nucleation parameterizations (i.e., N12 and CNT) in B14_N12_M18
382 and B14_CNT_M18 by comparing them with the B14_D15_M18 experiment,
383 respectively.

384 **3 Results**

385 **3.1 Evaluation of modeled MOA**

386 Given that a realistic representation of MOA emissions is a prerequisite for
387 models to quantify its influence on ice nucleation, we evaluate three different MOA



388 emission parameterizations in this section. We also analyze the processes contributing to
389 MOA burden such as emission, transport, and removal, because the burden pattern
390 largely determines the INP distribution pattern. Comparisons with available observations
391 are made to examine the performance of different MOA emission schemes.

392 Table 5 lists the annual global mean emissions and burdens of MOA and sea salt
393 from different simulations. Overall, the G11 method generates the largest global MOA
394 emission (27.1 Tg yr^{-1}) followed by the B14 method (24.5 Tg yr^{-1}). The magnitudes of
395 MOA emissions are within the range of previous studies (Huang et al., 2018; Meskhidze
396 et al., 2011; Langmann et al., 2008). The ratios of MOA emission to sea salt emission are
397 0.67% and 0.74% for the B14 and G11 experiments, respectively, which are also
398 comparable to previous studies ranging from 0.3% to 3.2% (Huang et al., 2018;
399 Meskhidze et al., 2011). The NULL approach only gives an annual global emission of 4.6
400 Tg yr^{-1} , with the ratio of MOA emission to sea salt emission of 0.13%. These values are
401 much lower than those of B14 and G11 approaches. We further evaluate aerosol mass
402 mixing ratios and number concentrations in each aerosol mode in the B14 experiment,
403 where MOA is added and internally mixed with sea salt. In B14, MOA comprises up to
404 70% and 50% of Aitken and accumulation mode SSA mass, respectively. Number
405 concentrations of accumulation mode aerosols near the surface are increased by up to 50%
406 over some regions of the Southern Ocean and Arctic.

407 Despite the fact that there are differences in the global annual mean value, B14
408 and G11 generate similar spatial patterns of MOA emission rates (Fig. 1), while G11
409 tends to give higher emission rates than B14. Large emission rates are located in the
410 mid-latitude storm tracks, equatorial upwelling, and coastal regions as shown in Fig. 1.
411 These locations largely reflect the geographic distribution of primary ocean productivity
412 as indicated by [Chl-a] (in G11) or organic matter concentrations (in B14).

413 Here we illustrate the influence of surface wind speeds (supplemental Fig. S1) on
414 the emission of MOA. Although high MOA emissions are mostly co-located with
415 vigorous oceanic biological activities, the oceanic area with smaller/larger wind speed
416 tends to have a decreased/elevated emission rate relative to their biological activities. For
417 instance, due to weak wind speeds ($\sim 5 \text{ m s}^{-1}$), a strong signal of oceanic organic matter
418 concentration does not correspond to a large emission rate in the west coast of South



419 America. On the contrary, because of strong wind speeds ($\sim 10 \text{ m s}^{-1}$), moderate emission
420 rates are noticed over the subtropical North Pacific Ocean and subtropical South Indian
421 Ocean despite relatively small [Chl-a] or organic matter concentrations. This wind speed
422 dependent pattern is more clearly shown in the B14 results than in the G11 results,
423 because in the B14 emission scheme, $F_{MOA/SSA}$ is not related to the wind speed while
424 SSA emission is proportional to the surface wind speed, as described in section 2.2.1.
425 Conversely, $F_{MOA/SSA}$ is inversely related to the wind speed in G11, results in a more
426 complicated relationship between wind speed and MOA emission rate in G11.

427 The global mean MOA burden is 0.097 Tg in B14, which is in close agreement
428 with previous studies which suggested a range of 0.031 to 0.131 Tg (Huang et al., 2018;
429 Burrows et al., 2018). The global distribution of MOA column burden shares the similar
430 patterns between G11 and B14, with the peak burden around 1 mg m^{-2} over the mid-to
431 high latitude Southern Ocean (Fig. 1). Despite the fact that large burdens are usually
432 related to locations of high emissions, they are also influenced by advection (dependent
433 on 3-D wind), dry deposition (dependent on particle size), and wet deposition (dependent
434 on precipitation). The oceanic regions with small annual precipitation rates (supplemental
435 Fig. S1) lead to considerable accumulations of MOA in G11 and B14. For instance, the
436 peak burdens with maximum values of 0.4 to 0.6 mg m^{-2} , on either side of the Pacific
437 tropical convection zone correspond to the subsidence induced dry zone (i.e., subsiding
438 branch of Walker and Hadley circulations).

439 Zonally-averaged vertical distributions of MOA mass mixing ratio illustrate the
440 vertical transport of MOA (Fig. 1). Simulations from G11 and B14 exhibit a maximum
441 value of $0.35 \text{ } \mu\text{g kg}^{-1}$ within the boundary layer, located in 40° – 50° S of the Southern
442 Ocean, while the maximum value is only $0.05 \text{ } \mu\text{g kg}^{-1}$ in NULL. Globally, G11 shows
443 slightly higher MOA mass mixing ratios over all latitudes compared with B14, and
444 transports more MOA to high altitudes over the tropical regions. It is clear that MOA is
445 accumulated in the lower troposphere, i.e. below 600 hPa in G11 and B14, and below 800
446 hPa in NULL. The reason is that MOA is generated over the oceans, especially over the
447 storm track regions with high precipitation, limiting MOA mainly to the lower
448 troposphere.



449 We further evaluate model simulated MOA concentrations with measurements at
450 Mace Head (Ireland) and Amsterdam Island (Fig. 2). The B14 and G11 methods do well
451 in capturing the observed seasonal variation of MOA concentrations at Amsterdam Island
452 (Fig. 2a), although the model produces slightly higher MOA concentrations. At Mace
453 Head, the two methods produce delayed concentration peaks by about one month
454 compared with observations (Fig. 2b). The mass fraction of MOA in SSA (Fig. 2c) shows
455 a better agreement between the model and observation. Both the simulated and observed
456 organic mass fraction increase from March and reaches a peak in July, although the
457 observed peak is broader. The NULL approach does not reproduce observed seasonal
458 cycles of MOA and significantly underestimates observed MOA concentrations due to
459 the prescribed mass fraction (0.05) in the accumulation mode.

460 Based on our analyses and comparisons with observations, we show that B14
461 implementation of MOA emission into CAM6 reasonably captures the concentrations and
462 seasonal variations of MOA. Next we will study the MOA effects on clouds with a focus
463 on its INP effect, based on model experiments with the B14 emission (Table 4).

464 **3.2 Impact of MOA on CCN**

465 After introducing MOA in the model, we notice an obvious increase in oceanic
466 surface CCN concentrations at high latitudes. Figure 3 shows the spatial distribution of
467 annual mean percentage changes in surface CCN concentrations at a supersaturation of
468 0.1% due to MOA, derived from the two experiments (CTL and B14_D15). From Fig. 3,
469 the annual mean CCN concentration increases by 15%–35% over much of the oceans
470 from 30°S to 70°S, with a maximum increase of 45% located over the Southern Ocean
471 (60°S, 55°E). Other regions showing significant increases of CCN are over the pristine
472 high latitudes, with increases of 25–35% from 60°S to Antarctica in the SH and from
473 60°N to 80°N in the NH. These results are comparable with previous results with an
474 average increase by 12% and up to 20% of CCN over the Southern Ocean (Meskhidze et
475 al., 2011). Over low- and mid-latitude oceans, CCN changes due to MOA are smaller.
476 Generally, the distribution of CCN change is consistent with the MOA emission pattern.
477 The vertical profiles of CCN concentrations from the two model experiments and
478 observations during the eight field campaigns are shown in Fig. 3. Clear increases of



479 CCN concentrations in the boundary layer due to MOA are evident for campaigns over
480 the ocean or coastal regions (SOCEX1, SOCEX2, ACE1, FIRE1, and ASTEX), with a
481 maximum increase (26%) in ACE1. Observed CCN from FIRE1 shows a strong
482 inversion of CCN below 800 hPa, and this inversion is challenging for the model due to
483 its coarse vertical resolution. An obvious underestimation of CCN in the model is noticed
484 at FIRE3 over the Arctic Ocean in Spring, which is attributed to the underestimated
485 transport of air pollution caused by too strong wet scavenging in the model (Liu et al.,
486 2012).

487 **3.3 Impact of MOA on INPs**

488 In order to examine the importance of MOA INPs, we compare modeled INPs
489 from MOA versus dust as well as compare them with observations from several field
490 campaigns in high latitudes (Fig. 4). Modeled INP concentrations from MOA are
491 calculated online using M18 and W15 parameterizations (from B14_D15_M18 and
492 B14_D15_W15 experiments, respectively), while dust INP concentrations are calculated
493 online using D15, CNT, and N12 parameterizations (from B14_D15_M18,
494 B14_CNT_M18, and B14_N12_M18 experiments, respectively). Modeled INP
495 concentrations are computed based on aerosol concentrations at different temperatures
496 and are selected at the same altitudes and locations as the observations. The measured
497 INP data were obtained from Mace Head, the CAPRICORN campaign (Clouds, Aerosols,
498 Precipitation, Radiation, and Atmospheric Composition over the Southern Ocean),
499 Oliktok Point, Zeppelin, and the SOCRATES campaign (Southern Ocean Clouds,
500 Radiation, Aerosol Transport Experimental Study) (McCluskey et al., 2018a; McCluskey
501 et al., 2018b; Creamean et al., 2018; Tobo et al., 2019).

502 As illustrated in Fig. 4, the M18 parameterization tends to underestimate observed
503 INP concentrations except at temperatures colder than -25°C . On the other hand, the W15
504 parameterization overestimates observed INP concentrations except at temperatures
505 warmer than -20°C . Under the same MOA scenario, the W15 parameterization is more
506 efficient in producing INPs than M18. This is because the M18 parameterization was
507 derived from MOA in the atmosphere which accounts for the effect of physiochemical
508 selective emission and aerosol chemistry in the air. In contrast, the W15 parameterization



509 was derived based on the total organic carbon in sea surface microlayer samples, which
510 contain higher organic mass concentrations compared with ambient MOA.

511 The dust INP concentration calculated with CNT shows an underestimation when
512 temperature is warmer than -20°C and an overestimation when temperature is between
513 -30°C and -20°C . This is consistent with previous work by Wang et al. (2014). The D15
514 parameterization indicates a clear underestimation. Meanwhile, the N12 parameterization
515 reveals an overall overprediction of INPs compared with observations. These results
516 suggest that the N12 parameterization is more efficient in producing dust INPs than the
517 D15 parameterization under the same dust loading. INP concentrations from N12 are
518 calculated based on the coarse, accumulation, and Aitken mode dust aerosol, which
519 account for fine dust particles, while INP concentrations from D15 are calculated based
520 on the number concentration of dust particles with diameters larger than $0.5\ \mu\text{m}$ (DeMott
521 et al., 2015). Simulated total INPs, the sum of dust and MOA INPs from D15 and M18,
522 gives a better agreement with observations than D15 and M18 alone, although
523 underestimations still exist at warmer temperatures.

524 Fig. 5 shows the comparison between simulated and measured INPs from five
525 parameterization schemes as a function of temperature for the same field campaigns as in
526 Fig. 4. Generally, an inverse linear relationship is revealed between $\log_{10}(\text{INPs})$ and
527 temperature in the measurements. This relationship is also shown in simulated INP number
528 concentrations from the empirical parameterizations (N12, D15, W15, M18). However, for
529 CNT, nearly constant INP number concentrations are presented at temperatures from
530 -35°C to -20°C , and then a rapid decrease with increasing temperature when temperature
531 is warmer than -20°C . At temperatures higher than -15°C , nearly no INPs are produced by
532 CNT, leading to the underestimation of INPs in the CNT method at these temperatures.

533 We notice higher INP number concentrations are produced from M18 compared
534 with W15 at Zeppelin during March 2017. The most distinctive feature of this campaign is
535 its very low aerosol loadings. For example, simulated SSA mass mixing ratio is around 0.6
536 $\mu\text{g kg}^{-1}$ with the maximum value at $1.8\ \mu\text{g kg}^{-1}$ below $850\ \text{hPa}$, and the dust mass mixing
537 ratio is around $0.3\ \mu\text{g kg}^{-1}$. We note that simulated dust INP number concentrations from
538 N12 are always higher than those from D15, and both N12 and D15 are more efficient in
539 producing INPs than CNT when temperature is warmer than -20°C .



540 The global distribution pattern of annual mean MOA INP concentrations at 950
541 hPa at temperature of -25°C is similar to that of MOA column burden concentrations, as
542 shown in Fig. 6a. The MOA INPs are spread over the oceans, with peaks ($\sim 0.1 \text{ L}^{-1}$) over
543 40°S to 60°S of the Southern Ocean, the subtropical Southern Indian Ocean, the
544 subtropical Atlantic Ocean, and the subtropical Eastern Pacific Ocean. Meanwhile, dust
545 INP concentrations diagnosed at the same pressure and at the same temperature (Fig. 6b)
546 are dominant over the NH and downwind of dust source regions in the SH (e.g., around
547 Australia and extended to 50°S).

548 Fig. 6c shows the horizontal distribution of ratio of MOA INP concentration to
549 dust INP concentration at 950 hPa. It is clear that MOA INPs are more important than
550 dust INPs in the 40°S south of SH, where MOA INP concentrations can reach up to 1000
551 times higher than those of dust INPs. The zonal mean vertical distribution of ratio of
552 MOA INP concentration to dust INP concentration is illustrated in Fig. 6d. The ratio
553 peaks near 65°S , indicating that MOA INPs are more important than dust INPs over the
554 Southern Ocean from surface up to 400 hPa, and extends poleward to 90°S . Above the
555 400 hPa altitude, dust particles are still more important INPs. Because dust particles are
556 emitted over drier deserts (i.e., with lower precipitation and thus less wet scavenging),
557 dust can be subject to long-range transport at high elevations. In contrast, most MOA
558 particles are generated over the storm track regions with high occurrences of precipitation.
559 Taking into account of emission, transport and wet scavenging of MOA and dust particles
560 results in MOA INPs dominating below 400 hPa over the Southern Ocean while dust
561 INPs are generally more important elsewhere.

562 Immersion freezing on MOA in mixed-phase clouds requires that there are cloud
563 droplets at temperatures colder than -4°C . Ice nucleation consumes cloud liquid water, and
564 thus will compete with other processes for cloud liquid water (e.g., autoconversion of
565 cloud water to rain, accretion of cloud water by rain and snow). This competition is
566 expected to result in a reduction of ice nucleation rate of MOA compared with the offline
567 calculation of ice nucleation rate as in McCluskey et al. (2019). Fig. 7 shows the annual
568 zonal mean ice production rates from the immersion freezing of MOA and dust, which are
569 calculated online for the cloud ice production tendency in the B14_D15_M18 experiment.
570 Over the NH, the immersion freezing of dust dominates the primary ice production, giving



571 an averaged ice production rate at $5 \text{ kg}^{-1}\text{s}^{-1}$ and up to $20 \text{ kg}^{-1}\text{s}^{-1}$ over 40°N at 400 hPa (Fig.
572 7b), while the MOA ice production rate is around $1 \text{ kg}^{-1}\text{s}^{-1}$ (Fig. 7a). However, in the
573 Arctic boundary layer, the MOA fraction of total ice production rate is around 0.6–0.7 (Fig.
574 7c), indicating that MOA INPs are more important in generating ice crystals than dust INPs
575 there. Over the SH, the immersion freezing rate of MOA dominates the primary ice
576 production below 400 hPa with the MOA fraction close to 1. The zonal average ice
577 nucleation rate of MOA is around $1 \text{ kg}^{-1}\text{s}^{-1}$, and up to $5 \text{ kg}^{-1}\text{s}^{-1}$ over the 65°S Southern
578 Ocean at 400–600 hPa. The immersion freezing rate of dust is around $1 \text{ kg}^{-1}\text{s}^{-1}$ above 500
579 hPa, and smaller than $0.1 \text{ kg}^{-1}\text{s}^{-1}$ below 600 hPa altitude in the SH. Analysis of the seasonal
580 variation of ice nucleation rate of MOA indicates that a maximum rate of about $16 \text{ kg}^{-1}\text{s}^{-1}$
581 occurs at 400–600 hPa over 60°S in July (austral winter). In summary, the annual mean
582 immersion freezing of MOA dominates the primary ice production over the SH below 400
583 hPa altitude and in the Arctic boundary layer.

584 **3.4 Impact of MOA on clouds and radiative forcing**

585 Table 6 displays the differences of cloud and precipitation variables between the
586 CTL and B14_D15_M18 experiments. With added MOA aerosol, the global annual mean
587 surface concentration of CCN at 0.1% supersaturation changes from 103.3 cm^{-3} in CTL to
588 106.6 cm^{-3} in B14_D15_M18. This increase of 3.28 cm^{-3} is comparable to other model
589 estimates of 3.66 cm^{-3} (Burrows et al., 2018), and $2.6\text{--}3.0 \text{ cm}^{-3}$ (Meskhidze et al., 2011).
590 The vertically-integrated cloud droplet number concentration (CDNUMC) increases by
591 5.25% in B14_D15_M18 compared with CTL, and by up to 16.89% over $20\text{--}90^\circ\text{S}$ during
592 the austral summer (December-January-February). The global annual mean liquid water
593 path (LWP), ice water path (IWP), longwave cloud forcing (LWCF), and total cloud
594 fraction (CLDTOT) do not show obvious changes between CTL and B14_D15_M18. The
595 global annual mean shortwave cloud forcing is stronger by -0.41 W m^{-2} due to MOA.
596 During the austral summer over $20\text{--}90^\circ\text{S}$, we notice an increase of 4.57 g m^{-2} (5.10%) in
597 LWP, and a 1.35% (2.52%) increase in low-cloud fraction. As a consequence, SWCF is
598 enhanced by -2.87 W m^{-2} (Table 6), which is comparable to -3.5 W m^{-2} estimated in
599 Burrows et al. (2018). Ice number concentration on -15°C isotherm increases by 9.34%



600 during the austral winter. There does not appear to be a significant change in LWCF, which
601 is consistent with the result of Huang et al. (2018).

602 Strong CCN effect of MOA on clouds (in terms of significant changes in CCN and
603 CDNUMC) tends to occur only in the SH over 40–60°S, while strong INP effect (in terms
604 of significant changes in cloud ice mass and number concentrations) is notable over 50–70°
605 in both Hemispheres (Fig. 8). Over 40–60°S, a significant increase from 70 to 90 cm⁻³ in
606 the annual zonal mean surface CCN concentration is observed. The CCN concentration
607 there is nearly 30% higher in B14_D15 and B14_D15_M18 than in CTL. As a result,
608 CDNUMC increases from 2.6×10^{10} m⁻² in CTL to 3.0×10^{10} m⁻² in B14_D15 and
609 B14_D15_M18 over 40–60°S, leading to an increase in LWP due to the aerosol indirect
610 effect (Fig. 8). Furthermore, we notice a stronger SWCF at 40–60°S by 3 W m⁻² in
611 B14_D15 compared with CTL. After considering the INP effect of MOA in the model, we
612 notice that cloud ice number concentration and cloud ice mass mixing ratio increase in
613 mixed-phase clouds which led to a slightly decrease in CDNUMC. As indicated in Fig.
614 8b,d, cloud ice number concentration increases from 4500 kg⁻¹ in B14_D15 to 5500 kg⁻¹ in
615 B14_D15_M18 at ~60°S, with cloud ice mass mixing ratio increased by 0.25 mg kg⁻¹.
616 Over 60°N, cloud ice number concentration increases from 4200 kg⁻¹ in B14_D15 to 5200
617 kg⁻¹ in B14_D15_M18, with cloud ice mass mixing ratio increased by 0.1 mg kg⁻¹.

618 Fig. 9 shows the seasonal variations of cloud properties and cloud radiative forcing
619 averaged over the 20°S–90°S in SH, in response to the introduction of MOA as CCN and
620 INPs. The seasonal variation of surface CCN concentration at 0.1% supersaturation shows
621 the maximum value of 72 cm⁻³ in the austral summer and the minimum value of ~50 cm⁻³
622 in the austral winter in CTL. Similar seasonal variation patterns are also noted for
623 CDNUMC and LWP. With the inclusion of MOA in the model, B14_D15 and
624 B14_D15_M18 produce more surface CCN, with an increase of up to 14 cm⁻³ (~20%) in
625 January, compared with CTL. Accordingly, CDNUMC increases from 2.1×10^{10} m⁻² in
626 CTL to 2.5×10^{10} m⁻² in B14_D15 in January, and LWP increases from 93 g m⁻² in CTL to
627 97 g m⁻² in B14_D15 in January. As a consequence, SWCF is stronger by -3.5 W m⁻² in
628 B14_D15 compared with CTL during the austral summer. We also notice that CCN,
629 CDNUMC, and SWCF show smaller changes during the austral winter due to weaker
630 oceanic biological activity.



631 Different from the warm cloud features above, seasonal variations of ice properties in
632 mixed-phase clouds (i.e., cloud ice mass mixing ratio and number concentration on -15°C
633 isotherm, IWP) clearly show winter maxima. After introducing the INP effect of MOA in
634 the model, ice number concentration on -15°C isotherm increases by comparing B14_D15
635 with B14_D15_M18, with obvious increases of up to 27% in June. Ice mass mixing ratio
636 on -15°C isotherm increases by 0.19 mg kg^{-1} (13%) in June. Increases in both cloud ice
637 number and mass contribute to the increase of IWP by 0.5 g m^{-2} in austral winter. The
638 seasonal change of LWCF is not well correlated with changes in ice number concentration
639 and mass mixing ratio in mixed-phase clouds, because LWCF is controlled more by high
640 clouds. Our introduction of MOA INPs mainly occurs in mixed-phased clouds, and
641 therefore has a small influence on LWCF.

642 As shown in Table 7, the CCN effect of MOA on SWCF is strongest in the austral
643 summer, with the value of -2.78 W m^{-2} over the 20°S – 90°S in SH. In contrast, the INP
644 effect of MOA on LWCF is strongest in the austral winter, with the value of 0.35 W m^{-2}
645 (Table 8). For the net cloud forcing (SWCF + LWCF), the CCN effect of MOA is 2.65 W m^{-2}
646 in the austral summer, and the INP effect is 0.65 W m^{-2} in austral spring over the
647 20°S – 90°S . The annual global mean CCN and INP effects of MOA on the net cloud
648 forcing are -0.35 and 0.016 W m^{-2} , respectively. From an annual mean perspective, the
649 CCN effect of MOA on SWCF is -0.84 W m^{-2} over 20 – 90°S and is about twice as much as
650 the global mean value (-0.41 W m^{-2}), which indicates that the global annual mean SWCF
651 change due to MOA is dominated by SH contributions.

652 **4 Discussion**

653 In this study, for the MOA emission process, we only considered the generation
654 of MOA during the film drop breakup in B14, and the generation of MOA from jet drops
655 is not currently included. The film drops form from bubble-cap films bursting, while the
656 jet drops generate from the base of breaking bubbles. Particles from jet drops, with the
657 diameter is around supermicrometer, are considered larger than particles from film drops
658 (Wang et al., 2017). Extending the current emission scheme to include MOA emissions
659 through jet drops (Wang et al., 2017) may be possible with more measurements and an



660 improved understanding of physical mechanisms that determine the sea spray organic
661 emission.

662 For the ice nucleation efficiency of MOA, the M18 parameterization only
663 includes the more persistent, heat-stable component observed in ambient sea spray
664 aerosol INP sampling. This neglects the heat-labile organic INPs (McCluskey et al.,
665 2018b). Regarding ice nucleation mechanisms, only the immersion mode of ice
666 nucleation is implemented in this study, however, recent laboratory experiments (Wolf et
667 al., 2019) have indicated a potentially important role of MOA in the deposition mode at
668 temperatures below -40°C . Future work will focus on improving the limitations of the
669 current understanding of MOA emission and ice nucleation in the model.

670 Recent studies indicated an underestimation of ice formation in CAM6
671 (D'Alessandro et al., 2019) that results in too much cloud liquid and too little cloud ice in
672 mixed-phase clouds. In addition to ice nucleation undertaken in this study, other factors
673 may contribute to this model bias. For example, the CLUBB scheme used in CAM6 for
674 turbulence and shallow convection treats only liquid phase condensation, lacking ice
675 formation in the model's large-scale cloud macrophysics (Zhang et al., 2020).
676 Furthermore, CAM6 misses the representation of several important mechanisms of
677 secondary ice formation. Observed secondary ice formation processes include rime
678 splintering, ice-ice collision fragmentation, droplet shattering during freezing, and
679 fragmentation during sublimation of ice bridges (Field et al., 2017). Currently, only the
680 rime splintering is considered in CAM6. Lastly, CAM6 with a horizontal resolution of
681 approximately 100 km may not resolve the subgrid cloud processes and heterogeneous
682 distributions of cloud hydrometeors (Tan et al., 2016; Zhang et al., 2019). These issues
683 will be addressed in future studies.

684 **5 Summary and Conclusions**

685 This study introduces MOA into CAM6 as a new aerosol species and treats the
686 chemistry, advection, and wet/dry deposition of MOA in the model. This paper also
687 considers the MOA influences on droplet activation and ice nucleation, particularly
688 focusing on quantifying the INP effect of MOA on cloud properties and radiation. Here
689 we summarize our main findings:



690 (1) Three different emission schemes (B14, G11, and NULL) of MOA were
691 implemented in the model and simulated MOA concentrations were evaluated with
692 available observations. The global simulation indicates that high MOA burden centers are
693 mostly co-located with regions of vigorous oceanic biological activities and high wind
694 speeds such as in mid-latitude storm tracks, the equatorial upwelling, and coastal regions.
695 The global MOA emission is 24.5 Tg yr^{-1} in B14, 27.1 Tg yr^{-1} in G11, and 4.6 Tg yr^{-1} in
696 the NULL emission approach. On the global scale, the MOA mass emission is 0.67%,
697 0.74%, and 0.13% of the sea salt mass emission from B14, G11, and NULL, respectively.
698 We show that observed seasonal cycles of marine organic matter at Mace Head and
699 Amsterdam Island are reproduced when the MOA fraction of SSA is assumed to depend
700 on sea spray biology (B14, G11), but are not reproduced when this fraction is assumed to
701 be constant (NULL). Our study does not support the constant organic mass fraction of
702 SSA emissions (Quinn et al., 2014; Saliba et al., 2019; Bates et al., 2020).

703 (2) After introducing MOA in the model, annual mean CCN concentrations (at
704 supersaturation of 0.1%) are increased by 15%–30% over the oceans ranging from 30°S
705 to 70°S . Two different ice nucleation schemes of MOA (M18 and W15) are implemented
706 and compared with available measurements. The INPs from MOA by the M18
707 parameterization show a reasonable agreement with observations at NH and SH high
708 latitudes, while simulated total INPs, the sum of MOA INPs from M18 and dust INPs
709 from D15, give a better agreement with observations. W15 for MOA alone overestimates
710 the observed INP concentrations across all temperatures. At -25°C , MOA INP
711 concentrations can be 1000 times higher than those of dust INPs over 40° – 60°S in the SH
712 boundary layer while dust INP concentrations are higher above 400 hPa altitude over SH
713 and NH.

714 (3) We notice a strong CCN effect of MOA over 40° – 60°S only in SH, while a
715 strong INP effect of MOA is identified over 50° – 70° in both Hemispheres. For seasonal
716 variations, CCN effect is stronger during the austral summer than winter, while INP
717 effect is stronger in the austral winter than summer. The CCN effect of MOA on SWCF
718 is strongest in the austral summer over SH with a value of -2.78 W m^{-2} , while the INP
719 effect on LWCF is strongest in the austral winter over SH with a value of 0.35 W m^{-2} .
720 The annual global mean CCN and INP effect of MOA on the net cloud forcing is -0.35 and



721 0.016 W m⁻², respectively. This work is a stepping stone towards better climate models
722 because the important role of MOA in biogeochemistry, hydrological cycle, and climate
723 change.

724

725

726 **Competing interests:** The authors declare that they have no conflict of interest.

727

728 **Data availability:** The model code is available at

729 <https://github.com/CESM-Development>. The observed INP data is available at

730 https://data.eol.ucar.edu/master_lists/generated/socrates/.

731

732 **Author contributions:** XZ and XL conceptualized the analysis and wrote the manuscript

733 with input from the co-authors. XZ modified the code, carried out the simulations, and

734 performed the analysis. SB provided scientific suggestions to the manuscript and

735 provided the model code for the emission of marine organic aerosol. YS provided help in

736 setting up the global climate model, designing the model runs, and created Figures. XL

737 was involved with obtaining the project grant, supervised the study. All authors were

738 involved in helpful discussions and contributed to the manuscript.

739

740 **Acknowledgment:** This research was supported by the DOE Atmospheric System

741 Research (ASR) Program (grant DE-SC0020510). S. M. Burrows was also funded by the

742 U.S. DOE Early Career Research Program. We thank Christina McCluskey for providing

743 the INP data from the SOCRATES campaign.



744 References

- 745 Abdul-Razzak, H., and Ghan, S. J.: A parameterization of aerosol activation 2. Multiple aerosol types,
746 *Journal of Geophysical Research Atmospheres*, 105, 6837-6844, 10.1029/1999JD901161, 2000.
- 747 Alpert, P. A., Kilhau, W. P., Bothe, D. W., Radway, J. A. C., Aller, J. Y., and Knopf, D. A.: The influence
748 of marine microbial activities on aerosol production: A laboratory mesocosm study, *Journal of*
749 *Geophysical Research*, 120, 8841-8860, 10.1002/2015JD023469, 2015.
- 750 Ault, A. P., Moffet, R. C., Baltrusaitis, J., Collins, D. B., Ruppel, M. J., Cuadra-Rodriguez, L. A., Zhao, D.,
751 Guasco, T. L., Ebben, C. J., Geiger, F. M., Bertram, T. H., Prather, K. A., and Grassian, V. H.:
752 Size-dependent changes in sea spray aerosol composition and properties with different seawater
753 conditions, *Environmental Science and Technology*, 47, 5603-5612, 10.1021/es400416g, 2013.
- 754 Bates, T. S., Quinn, P. K., Coffman, D. J., Johnson, J. E., Upchurch, L., Saliba, G., Lewis, S., Graff, J.,
755 Russell, L. M., and Behrenfeld, M. J.: Variability in Marine Plankton Ecosystems Are Not Observed
756 in Freshly Emitted Sea Spray Aerosol Over the North Atlantic Ocean, *Geophys Res Lett*, 47,
757 10.1029/2019GL085938, 2020.
- 758 Bigg, E. K.: The formation of atmospheric ice crystals by the freezing of droplets, *Quarterly Journal of the*
759 *Royal Meteorological Society*, 79(342), 510–519, doi:10.1002/qj.49707934207, 1953.
- 760 Burrows, S. M., Easter, R., Liu, X., Ma, P. L., Wang, H., Elliott, S. M., Singh, B., Zhang, K., and Rasch, P.
761 J.: OCEANFILMS sea-spray organic aerosol emissions – Part 1: implementation and impacts on
762 clouds, *Atmos. Chem. Phys. Discuss.*, 2018, 1-27, 10.5194/acp-2018-70, 2018.
- 763 Burrows, S. M., Ogunro, O., Frossard, A. A., Russell, L. M., Rasch, P. J., and Elliott, S. M.: A physically
764 based framework for modeling the organic fractionation of sea spray aerosol from bubble film
765 Langmuir equilibria, *Atmos Chem Phys*, 14, 13601-13629, 2014.
- 766 Ceburnis, D., O'Dowd, C. D., Jennings, G. S., Facchini, M. C., Emblico, L., Decesari, S., Fuzzi, S., and
767 Sakalys, J.: Marine aerosol chemistry gradients: Elucidating primary and secondary processes and
768 fluxes, *Geophys Res Lett*, 35, 2008.
- 769 Christiansen, S., Salter, M. E., Gorokhova, E., Nguyen, Q. T., and Bilde, M.: Sea Spray Aerosol Formation:
770 Laboratory Results on the Role of Air Entrainment, Water Temperature, and Phytoplankton Biomass,
771 *Environmental Science and Technology*, 10.1021/acs.est.9b04078, 2019.
- 772 Creamean, J. M., Kirpes, R. M., Pratt, K. A., Spada, N. J., Maahn, M., De Boer, G., Schnell, R. C., and
773 China, S.: Marine and terrestrial influences on ice nucleating particles during continuous springtime
774 measurements in an Arctic oilfield location, *Atmos Chem Phys*, 18, 18023-18042,
775 10.5194/acp-18-18023-2018, 2018.
- 776 Cullen, J. J.: The Deep Chlorophyll Maximum: Comparing Vertical Profiles of Chlorophyll a, *Canadian*
777 *Journal of Fisheries and Aquatic Sciences*, 39, 791-803, 10.1139/f82-108, 1982.
- 778 D'Alessandro, J. J., Diao, M., Wu, C., Liu, X., Jensen, J. B., and Stephens, B. B.: Cloud phase and relative
779 humidity distributions over the Southern Ocean in austral summer based on in situ observations and
780 CAM5 simulations, *Journal of Climate*, 32, 2781-2805, 10.1175/JCLI-D-18-0232.1, 2019.
- 781 DeMott, P. J., Hill, T. C. J., McCluskey, C. S., Prather, K. A., Collins, D. B., Sullivan, R. C., Ruppel, M. J.,
782 Mason, R. H., Irish, V. E., Lee, T., Hwang, C. Y., Rhee, T. S., Snider, J. R., McMeeking, G. R.,
783 Dhaniyala, S., Lewis, E. R., Wentzell, J. J. B., Abbatt, J., Lee, C., Sultana, C. M., Ault, A. P., Axson, J.
784 L., Martinez, M. D., Venero, I., Santos-Figueroa, G., Stokes, M. D., Deane, G. B., Mayol-Bracero, O.
785 L., Grassian, V. H., Bertram, T. H., Bertram, A. K., Moffett, B. F., and Franc, G. D.: Sea spray aerosol
786 as a unique source of ice nucleating particles, *P Natl Acad Sci USA*, 113, 5797-5803, 2016.
- 787 DeMott, P. J., Prenni, A. J., McMeeking, G. R., Sullivan, R. C., Petters, M. D., Tobo, Y., Niemand, M.,
788 Mohler, O., Snider, J. R., Wang, Z., and Kreidenweis, S. M.: Integrating laboratory and field data to



- 789 quantify the immersion freezing ice nucleation activity of mineral dust particles, *Atmos Chem Phys*,
790 15, 393-409, 2015.
- 791 Facchini, M. C., Rinaldi, M., Decesari, S., Carbone, C., Finessi, E., Mircea, M., Fuzzi, S., Ceburnis, D.,
792 Flanagan, R., Nilsson, E. D., de Leeuw, G., Martino, M., Woeltjen, J., and O'Dowd, C. D.: Primary
793 submicron marine aerosol dominated by insoluble organic colloids and aggregates, *Geophys Res Lett*,
794 35, 10.1029/2008GL034210, 2008.
- 795 Field, P. R., Lawson, R. P., Brown, P. R. A., Lloyd, G., Westbrook, C., Moisseev, D., Miltenberger, A.,
796 Nenes, A., Blyth, A., Choularton, T., Connolly, P., Buehl, J., Crosier, J., Cui, Z., Dearden, C., DeMott,
797 P., Flossmann, A., Heymsfield, A., Huang, Y., Kalesse, H., Kanji, Z. A., Korolev, A., Kirchgaessner,
798 A., Lasher-Trapp, S., Leisner, T., McFarquhar, G., Phillips, V., Stith, J., and Sullivan, S.: Chapter 7.
799 Secondary Ice Production - current state of the science and recommendations for the future,
800 *Meteorological Monographs*, 58, 7.1-7.20, 10.1175/amsmonographs-d-16-0014.1, 2016.
- 801 Forestieri, S. D., Moore, K. A., Martinez Borrero, R., Wang, A., Stokes, M. D., and Cappa, C. D.:
802 Temperature and Composition Dependence of Sea Spray Aerosol Production, *Geophys Res Lett*, 45,
803 7218-7225, 10.1029/2018GL078193, 2018.
- 804 Gantt, B., and Meskhidze, N.: The physical and chemical characteristics of marine primary organic aerosol:
805 a review, *Atmos Chem Phys*, 13, 3979-3996, 2013.
- 806 Gantt, B., Meskhidze, N., Facchini, M. C., Rinaldi, M., Ceburnis, D., and O'Dowd, C. D.: Wind speed
807 dependent size-resolved parameterization for the organic mass fraction of sea spray aerosol, *Atmos*
808 *Chem Phys*, 11, 8777-8790, 2011.
- 809 Gardner, W. D., Mishonov, A., and Richardson, M. J.: Global POC concentrations from in-situ and satellite
810 data, *Deep-Sea Res Pt II*, 53, 718-740, 2006.
- 811 Gettelman, A., and Morrison, H.: Advanced Two-Moment Bulk Microphysics for Global Models. Part I:
812 Off-Line Tests and Comparison with Other Schemes, *Journal of Climate*, 28, 1268-1287, 2015.
- 813 Golaz, J.-C., Larson, V. E., Cotton, W. R., Golaz, J.-C., Larson, V. E., and Cotton, W. R.: A PDF-Based
814 Model for Boundary Layer Clouds. Part I: Method and Model Description,
815 [http://dx.doi.org/10.1175/1520-0469\(2002\)059<3540:APBMFB>2.0.CO;2](http://dx.doi.org/10.1175/1520-0469(2002)059<3540:APBMFB>2.0.CO;2),
816 10.1175/1520-0469(2002)059<3540:APBMFB>2.0.CO;2, 2002.
- 817 Golaz, J. C., Caldwell, P. M., Van Roekel, L. P., Petersen, M. R., Tang, Q., Wolfe, J. D., Abeshu, G.,
818 Anantharaj, V., Asay-Davis, X. S., Bader, D. C., Baldwin, S. A., Bisht, G., Bogenschutz, P. A.,
819 Branstetter, M., Brunke, M. A., Brus, S. R., Burrows, S. M., Cameron-Smith, P. J., Donahue, A. S.,
820 Deakin, M., Easter, R. C., Evans, K. J., Feng, Y., Flanner, M., Foucar, J. G., Fyke, J. G., Griffin, B. M.,
821 Hannay, C., Harrop, B. E., Hoffman, M. J., Hunke, E. C., Jacob, R. L., Jacobsen, D. W., Jeffery, N.,
822 Jones, P. W., Keen, N. D., Klein, S. A., Larson, V. E., Leung, L. R., Li, H. Y., Lin, W., Lipscomb, W.
823 H., Ma, P. L., Mahajan, S., Maltrud, M. E., Mامتjanov, A., McClean, J. L., McCoy, R. B., Neale, R.
824 B., Price, S. F., Qian, Y., Rasch, P. J., Reeves Eyre, J. E. J., Riley, W. J., Ringler, T. D., Roberts, A. F.,
825 Roesler, E. L., Salinger, A. G., Shaheen, Z., Shi, X., Singh, B., Tang, J., Taylor, M. A., Thornton, P.
826 E., Turner, A. K., Veneziani, M., Wan, H., Wang, H., Wang, S., Williams, D. N., Wolfram, P. J.,
827 Worley, P. H., Xie, S., Yang, Y., Yoon, J. H., Zelinka, M. D., Zender, C. S., Zeng, X., Zhang, C.,
828 Zhang, K., Zhang, Y., Zheng, X., Zhou, T., and Zhu, Q.: The DOE E3SM Coupled Model Version 1:
829 Overview and Evaluation at Standard Resolution, *Journal of Advances in Modeling Earth Systems*, 11,
830 2089-2129, 10.1029/2018MS001603, 2019.
- 831 Hoose, C., and Mohler, O.: Heterogeneous ice nucleation on atmospheric aerosols: a review of results from
832 laboratory experiments, *Atmos Chem Phys*, 12, 9817-9854, 10.5194/acp-12-9817-2012, 2012.
- 833 Huang, W. T. K., Ickes, L., Tegen, I., Rinaldi, M., Ceburnis, D., and Lohmann, U.: Global relevance of
834 marine organic aerosol as ice nucleating particles, *Atmos Chem Phys*, 18, 11423-11445, 2018.
- 835 Iacono, M. J., Delamere, J. S., Mlawer, E. J., Shephard, M. W., Clough, S. A., and Collins, W. D.:
836 Radiative forcing by long-lived greenhouse gases: Calculations with the AER radiative transfer
837 models, *J Geophys Res-Atmos*, 113, 2008.



- 838 Iacono, M. J., Delamere, J. S., Mlawer, E. J., Shephard, M. W., Clough, S. A., and Collins, W. D.:
839 Radiative forcing by long-lived greenhouse gases: Calculations with the AER radiative transfer
840 models, *Journal of Geophysical Research Atmospheres*, 113, 10.1029/2008JD009944, 2008.
- 841 Kanji, Z. A., Ladino, L. A., Wex, H., Boose, Y., Burkert-Kohn, M., Cziczo, D. J., and Kramer, M.:
842 Overview of Ice Nucleating Particles, *Meteor Mon*, 58, 10.1175/Amsmonographs-D-16-0006.1, 2017.
- 843 Langmann, B., Scannell, C., and O'Dowd, C.: New Directions: Organic matter contribution to marine
844 aerosols and cloud condensation nuclei, *Atmos Environ*, 42, 7821-7822, 2008.
- 845 Larson, V. E., Golaz, J.-C., and Cotton, W. R.: Small-Scale and Mesoscale Variability in Cloudy Boundary
846 Layers: Joint Probability Density Functions, *Journal of the Atmospheric Sciences*, 59, 3519-3539,
847 10.1175/1520-0469(2002)059<3519:SSAMVI>2.0.CO;2, 2002.
- 848 Lin, S. J., and Rood, R. B.: An explicit flux-form semi-Lagrangian shallow-water model on the sphere, *Q J*
849 *Roy Meteor Soc*, 123, 2477-2498, 1997.
- 850 Liu, X., Easter, R. C., Ghan, S. J., Zaveri, R., Rasch, P., Shi, X., Lamarque, J. F., Gettelman, A., Morrison,
851 H., Vitt, F., Conley, A., Park, S., Neale, R., Hannay, C., Ekman, A. M. L., Hess, P., Mahowald, N.,
852 Collins, W., Iacono, M. J., Bretherton, C. S., Flanner, M. G., and Mitchell, D.: Toward a minimal
853 representation of aerosols in climate models: description and evaluation in the Community
854 Atmosphere Model CAM5, *Geosci Model Dev*, 5, 709-739, 2012.
- 855 Liu, X., Ma, P. L., Wang, H., Tilmes, S., Singh, B., Easter, R. C., Ghan, S. J., and Rasch, P. J.: Description
856 and evaluation of a new four-mode version of the Modal Aerosol Module (MAM4) within version 5.3
857 of the Community Atmosphere Model, *Geosci Model Dev*, 9, 505-522, 2016.
- 858 Martensson, E. M., Nilsson, E. D., de Leeuw, G., Cohen, L. H., and Hansson, H. C.: Laboratory
859 simulations and parameterization of the primary marine aerosol production, *J Geophys Res-Atmos*,
860 108, 2003.
- 861 McCluskey, C. S., DeMott, P. J., Ma, P. L., and Burrows, S. M.: Numerical Representations of Marine
862 Ice-Nucleating Particles in Remote Marine Environments Evaluated Against Observations, *Geophys*
863 *Res Lett*, 46, 7838-7847, 10.1029/2018gl081861, 2019.
- 864 McCluskey, C. S., Hill, T. C. J., Humphries, R. S., Rauker, A. M., Moreau, S., Stratton, P. G., Chambers, S.
865 D., Williams, A. G., McRobert, I., Ward, J., Keywood, M. D., Harnwell, J., Ponsonby, W., Loh, Z. M.,
866 Krummel, P. B., Protat, A., Kreidenweis, S. M., and DeMott, P. J.: Observations of Ice Nucleating
867 Particles Over Southern Ocean Waters, *Geophys Res Lett*, 45, 11,989-911,997,
868 10.1029/2018GL079981, 2018a.
- 869 McCluskey, C. S., Ovadnevaite, J., Rinaldi, M., Atkinson, J., Belosi, F., Ceburnis, D., Marullo, S., Hill, T.
870 C. J., Lohmann, U., Kanji, Z. A., O'Dowd, C., Kreidenweis, S. M., and DeMott, P. J.: Marine and
871 Terrestrial Organic Ice-Nucleating Particles in Pristine Marine to Continentally Influenced Northeast
872 Atlantic Air Masses, *J Geophys Res-Atmos*, 123, 6196-6212, 2018b.
- 873 Meskhidze, N., Xu, J., Gantt, B., Zhang, Y., Nenes, A., Ghan, S. J., Liu, X., Easter, R., and Zaveri, R.:
874 Global distribution and climate forcing of marine organic aerosol: 1. Model improvements and
875 evaluation, *Atmos Chem Phys*, 11, 11689-11705, 2011.
- 876 Meyers, M. P., Demott, P. J. and Cotton, W. R.: New primary ice-nucleation parameterizations in an
877 explicit cloud model, *Journal of Applied Meteorology*, 31(7), 708-721,
878 doi:10.1175/1520-0450(1992)031<0708:NPINPI>2.0.CO;2, 1992.
- 879 Mlawer, E. J., Taubman, S. J., Brown, P. D., Iacono, M. J., and Clough, S. A.: Radiative transfer for
880 inhomogeneous atmospheres: RRTM, a validated correlated-k model for the longwave, *J Geophys*
881 *Res-Atmos*, 102, 16663-16682, 1997.
- 882 Murray, B. J., O'Sullivan, D., Atkinson, J. D., and Webb, M. E.: Ice nucleation by particles immersed in
883 supercooled cloud droplets, *Chem Soc Rev*, 41, 6519-6554, 10.1039/c2cs35200a, 2012.
- 884 Niemand, M., Möhler, O., Vogel, B., Vogel, H., Hoose, C., Connolly, P., Klein, H., Bingemer, H., DeMott,
885 P., Skrotzki, J., and Leisner, T.: A Particle-Surface-Area-Based Parameterization of Immersion



- 886 Freezing on Desert Dust Particles, *Journal of the Atmospheric Sciences*, 69, 3077-3092,
887 10.1175/JAS-D-11-0249.1, 2012.
- 888 O'Dowd, C. D., Facchini, M. C., Cavalli, F., Ceburnis, D., Mircea, M., Decesari, S., Fuzzi, S., Yoon, Y. J.,
889 and Putaud, J. P.: Biogenically driven organic contribution to marine aerosol, *Nature*, 431, 676-680,
890 2004.
- 891 O'Dowd, C. D., Langmann, B., Varghese, S., Scannell, C., Ceburnis, D., and Facchini, M. C.: A combined
892 organic-inorganic sea-spray source function, *Geophys Res Lett*, 35, 2008.
- 893 Prather, K. A., Bertram, T. H., Grassian, V. H., Deane, G. B., Stokes, M. D., DeMott, P. J., Aluwihare, L. I.,
894 Palenik, B. P., Azam, F., Seinfeld, J. H., Moffet, R. C., Molina, M. J., Cappa, C. D., Geiger, F. M.,
895 Roberts, G. C., Russell, L. M., Ault, A. P., Baltrusaitis, J., Collins, D. B., Corrigan, C. E.,
896 Cuadra-Rodriguez, L. A., Ebben, C. J., Forestieri, S. D., Guasco, T. L., Hersey, S. P., Kim, M. J.,
897 Lambert, W. F., Modini, R. L., Mui, W., Pedler, B. E., Ruppel, M. J., Ryder, O. S., Schoepp, N. G.,
898 Sullivan, R. C., and Zhao, D.: Bringing the ocean into the laboratory to probe the chemical complexity
899 of sea spray aerosol, *P Natl Acad Sci USA*, 110, 7550-7555, 10.1073/pnas.1300262110, 2013.
- 900 Quinn, P. K., Bates, T. S., Schulz, K. S., Coffman, D. J., Frossard, A. A., Russell, L. M., Keene, W. C., and
901 Kieber, D. J.: Contribution of sea surface carbon pool to organic matter enrichment in sea spray
902 aerosol, *Nat Geosci*, 7, 228-232, 10.1038/ngeo2092, 2014.
- 903 Rasch, P. J., Xie, S., Ma, P. L., Lin, W., Wang, H., Tang, Q., Burrows, S. M., Caldwell, P., Zhang, K.,
904 Easter, R. C., Cameron-Smith, P., Singh, B., Wan, H., Golaz, J. C., Harrop, B. E., Roesler, E.,
905 Bacmeister, J., Larson, V. E., Evans, K. J., Qian, Y., Taylor, M., Leung, L. R., Zhang, Y., Brent, L.,
906 Branstetter, M., Hannay, C., Mahajan, S., Mamejtanov, A., Neale, R., Richter, J. H., Yoon, J. H.,
907 Zender, C. S., Bader, D., Flanner, M., Foucar, J. G., Jacob, R., Keen, N., Klein, S. A., Liu, X.,
908 Salinger, A. G., Shrivastava, M., and Yang, Y.: An Overview of the Atmospheric Component of the
909 Energy Exascale Earth System Model, *Journal of Advances in Modeling Earth Systems*, 11,
910 2377-2411, 10.1029/2019MS001629, 2019.
- 911 Rastelli, E., Corinaldesi, C., Dell'anno, A., Lo Martire, M., Greco, S., Cristina Facchini, M., Rinaldi, M.,
912 O'Dowd, C., Ceburnis, D., and Danovaro, R.: Transfer of labile organic matter and microbes from the
913 ocean surface to the marine aerosol: An experimental approach, *Sci Rep-Uk*, 7, 1-10,
914 10.1038/s41598-017-10563-z, 2017.
- 915 Rinaldi, M., Fuzzi, S., Decesari, S., Marullo, S., Santolero, R., Provenzale, A., von Hardenberg, J., Ceburnis,
916 D., Vaishya, A., O'Dowd, C. D., and Facchini, M. C.: Is chlorophyll-a the best surrogate for organic
917 matter enrichment in submicron primary marine aerosol?, *J Geophys Res-Atmos*, 118, 4964-4973,
918 2013.
- 919 Saliba, G., Chen, C. L., Lewis, S., Russell, L. M., Rivellini, L. H., Lee, A. K. Y., Quinn, P. K., Bates, T. S.,
920 Haëntjens, N., Boss, E. S., Karp-Boss, L., Baetge, N., Carlson, C. A., and Behrenfeld, M. J.: Factors
921 driving the seasonal and hourly variability of sea-spray aerosol number in the North Atlantic, *P Natl
922 Acad Sci USA*, 116, 20309-20314, 10.1073/pnas.1907574116, 2019.
- 923 Schnell, R. C., and Vali, G.: Freezing nuclei in marine waters, *Tellus*, 27, 321-323,
924 10.3402/tellusa.v27i3.9911, 1975.
- 925 Sciare, J., Favez, O., Sarda-Estève, R., Oikonomou, K., Cachier, H., and Kazan, V.: Long-term
926 observations of carbonaceous aerosols in the Austral Ocean atmosphere: Evidence of a biogenic
927 marine organic source, *J Geophys Res-Atmos*, 114, 2009.
- 928 Shi, Y., and Liu, X.: Dust Radiative Effects on Climate by Glaciating Mixed-Phase Clouds, *Geophys Res
929 Lett*, 46, 6128-6137, 10.1029/2019GL082504, 2019.
- 930 Steele, J. H.: ENVIRONMENTAL CONTROL OF PHOTOSYNTHESIS IN THE SEA, *Limnology and
931 Oceanography*, 7, 137-150, 10.4319/lo.1962.7.2.0137, 1962.
- 932 Tobo, Y., Adachi, K., DeMott, P. J., Hill, T. C. J., Hamilton, D. S., Mahowald, N. M., Nagatsuka, N.,
933 Ohata, S., Uetake, J., Kondo, Y., and Koike, M.: Glacially sourced dust as a potentially significant
934 source of ice nucleating particles, *Nat Geosci*, 12, 253-+, 10.1038/s41561-019-0314-x, 2019.



- 935 Vergara-Temprado, J., Murray, B. J., Wilson, T. W., O'Sullivan, D., Browse, J., Pringle, K. J., Ardon-Dryer,
936 K., Bertram, A. K., Burrows, S. M., Ceburnis, D., DeMott, P. J., Mason, R. H., O'Dowd, C. D.,
937 Rinaldi, M., and Carslaw, K. S.: Contribution of feldspar and marine organic aerosols to global ice
938 nucleating particle concentrations, *Atmos Chem Phys*, 17, 3637-3658, 2017.
- 939 Vignati, E., Facchini, M. C., Rinaldi, M., Scannell, C., Ceburnis, D., Sciare, J., Kanakidou, M.,
940 Myriokefalitakis, S., Dentener, F., and O'Dowd, C. D.: Global scale emission and distribution of
941 sea-spray aerosol: Sea-salt and organic enrichment, *Atmos Environ*, 44, 670-677, 2010.
- 942 Wang, X., Deane, G. B., Moore, K. A., Ryder, O. S., Stokes, M. D., Beall, C. M., Collins, D. B., Santander,
943 M. V., Burrows, S. M., Sultana, C. M., and Prather, K. A.: The role of jet and film drops in controlling
944 the mixing state of submicron sea spray aerosol particles, *P Natl Acad Sci USA*, 114, 6978-6983,
945 10.1073/pnas.1702420114, 2017.
- 946 Wang, Y., Liu, X., Hoose, C., and Wang, B.: Different contact angle distributions for heterogeneous ice
947 nucleation in the Community Atmospheric Model version 5, *Atmos Chem Phys*, 14, 10411-10430,
948 2014.
- 949 Wilson, T. W., Ladino, L. A., Alpert, P. A., Breckels, M. N., Brooks, I. M., Browse, J., Burrows, S. M.,
950 Carslaw, K. S., Huffman, J. A., Judd, C., Kilhau, W. P., Mason, R. H., McFiggans, G., Miller, L. A.,
951 Najera, J. J., Polishchuk, E., Rae, S., Schiller, C. L., Si, M., Temprado, J. V., Whale, T. F., Wong, J. P.
952 S., Wurl, O., Yakobi-Hancock, J. D., Abbatt, J. P. D., Aller, J. Y., Bertram, A. K., Knopf, D. A., and
953 Murray, B. J.: A marine biogenic source of atmospheric ice-nucleating particles, *Nature*, 525, 234-+,
954 2015.
- 955 Wolf, M. J., Coe, A., Dove, L. A., Zawadowicz, M. A., Dooley, K., Biller, S. J., Zhang, Y., Chisholm, S.
956 W., and Cziczo, D. J.: Investigating the Heterogeneous Ice Nucleation of Sea Spray Aerosols Using
957 *Prochlorococcus* as a Model Source of Marine Organic Matter, *Environmental Science and*
958 *Technology*, 53, 1139-1149, 10.1021/acs.est.8b05150, 2019.
- 959 Yoon, Y. J., Ceburnis, D., Cavalli, F., Jourdan, O., Putaud, J. P., Facchini, M. C., Decesari, S., Fuzzi, S.,
960 Sellegri, K., Jennings, S. G., and O'Dowd, C. D.: Seasonal characteristics of the physicochemical
961 properties of North Atlantic marine atmospheric aerosols, *Journal of Geophysical Research*
962 *Atmospheres*, 112, 10.1029/2005JD007044, 2007.
- 963 Yun, Y. X., and Penner, J. E.: An evaluation of the potential radiative forcing and climatic impact of
964 marine organic aerosols as heterogeneous ice nuclei, *Geophys Res Lett*, 40, 4121-4126, 2013.
- 965 Zhang, G. J., and Mcfarlane, N. A.: Sensitivity of Climate Simulations to the Parameterization of Cumulus
966 Convection in the Canadian Climate Center General-Circulation Model, *Atmos Ocean*, 33, 407-446,
967 1995.
- 968 Zhang, M., Liu, X., Diao, M., D'Alessandro, J. J., Wang, Y., Wu, C., Zhang, D., Wang, Z., and Xie, S.:
969 Impacts of Representing Heterogeneous Distribution of Cloud Liquid and Ice on Phase Partitioning of
970 Arctic Mixed-Phase Clouds with NCAR CAM5, *Journal of Geophysical Research: Atmospheres*, 124,
971 13071-13090, 10.1029/2019JD030502, 2019.
- 972 Zhang, M., Xie, S., Liu, X., Lin, W., Zhang, K., Ma, H. Y., Zheng, X., and Zhang, Y.: Toward
973 Understanding the Simulated Phase Partitioning of Arctic Single-Layer Mixed-Phase Clouds in E3SM,
974 *Earth and Space Science*, 10.1029/2020ea001125, 2020.
- 975
- 976



Table 1. Aerosol species in MAM4 modes

	Accumulation	Aitken	Coarse	primary
Species	num_a1, so4_a1, pom_a1, soa_a1, bc_a1, dst_a1, ncl_a1, mom_a1	num_a2, so4_a2, soa_a2, ncl_a2, dst_a2, mom_a2	num_a3, dst_a3, ncl_a3, so4_a3	num_a4, pom_a4, bc_a4, (mom_a4 if internal added)
Size range	0.08 – 1 μm	0.02 – 0.08 μm	1–10 μm	0.08 – 1 μm
Standard Deviation σ	1.6	1.6	1.2	1.6
Number-median diameter D_{gn}	1.1×10^{-7}	2.6×10^{-8}	2.0×10^{-6}	5.0×10^{-8}
Low bound D_{gn}	5.35×10^{-8}	8.7×10^{-9}	1.0×10^{-6}	1.0×10^{-8}
High bound D_{gn}	4.4×10^{-7}	5.2×10^{-8}	4.0×10^{-6}	1.0×10^{-7}



Table 2. Aerosol species and physical properties

Species	Name	Density (kg m ⁻³)	Hygroscopicity
BC	Black carbon	1700	1.0×10^{-10}
SO4	Sulfate	1770	0.507
SOA	Secondary organic	1000	0.14
POA	Primary organic	1000	1.0×10^{-10}
DST	Dust	2600	0.068
NCL	Sea salt	1900	1.16
MOA	Marine organic aerosol	1601	0.1



Table 3. Molecular weights, mass at saturation, Langmuir parameters of the three ocean macromolecules

Species	polysaccharides	proteins	Lipids
Molecular weight [g mol ⁻¹]	250000	66463	284
mass per area at saturation [g m ⁻²]	0.1376	0.00219	0.002593
Langmuir parameter [m ³ mol ⁻¹]	90.58	25175	18205



Table 4. List of experiments to test model sensitivity to different emission and ice nucleation schemes

Name	Emission of MOA	DUST ice nucleation	MOA ice nucleation	Notes
BASE	—	CNT	—	Base line simulation
B14	Burrows et al. [2014]	CNT	—	Sensitivity test of emission scheme
G11	Gantt et al. [2011]	CNT	—	Sensitivity test of emission scheme
NULL	NULL	CNT	—	Sensitivity test of emission scheme
CTL		DeMott et al. [2015]		Control simulation
B14_D15	Burrows et al. [2014]	DeMott et al. [2015]		CCN effect
B14_D15_M18	Burrows et al. [2014]	DeMott et al. [2015]	McCluskey et al. [2018]	INP effect
B14_D15_W15	Burrows et al. [2014]	DeMott et al. [2015]	Wilson et al. [2015]	Sensitivity test of MOA INP parameterization
B14_N12_M18	Burrows et al. [2014]	Niemand et al. [2012]	McCluskey et al. [2018]	Sensitivity test of dust INP parameterization
B14_CNT_M18	Burrows et al. [2014]	CNT	McCluskey et al. [2018]	Sensitivity test of dust INP parameterization



Table 5. Annual global mean emissions and burdens of MOA and sea salt

Name	Sea salt emission ($Tg\ yr^{-1}$)	MOA emission ($Tg\ yr^{-1}$)	Sea salt burden (Tg)	MOA burden (Tg)	MOA/Sea salt emission (%)
BASE	3651	—	8.83	—	—
B14	3656	24.5	8.88	0.097	0.67
G11	3666	27.1	8.86	0.120	0.74
NULL	3648	4.6	8.85	0.018	0.13



1 Table 6. Mean changes and relative changes (%) between CTL and B14_D15_M18 experiments.
 2 Included in the table are surface CCN concentrations at 0.1% (CCN), ice particle number concentration at
 3 -15°C thermal level (Ni_{15}), vertically-integrated cloud droplet number concentration (CDNUMC), total
 4 grid-box cloud liquid water path (LWP), total grid-box cloud ice water path (IWP), shortwave and
 5 longwave cloud forcings (SWCF, LWCF), total cloud fraction (CLDTOT), high/mid-level/low-level clouds
 6 (CLDHGH, CLDMED, CLDLOW), and total surface precipitation rate (PRECT), with bold font indicating
 7 relative changes larger than 3%.
 8

	Global ANN	20S–90S ANN	20S–90S JJA	20S–90S DJF
CCN (cm^{-3})	3.28 (3.17)	4.85 (8.45)	1.37 (2.84)	9.26 (13.47)
Ni_{15} (m^{-3})	39.39 (2.25)	102.0 (5.21)	275.93 (9.34)	$-3.05 (-0.510)$
CDNUMC (cm^{-2})	7.53×10^4 (5.25)	1.27×10^5 (8.65)	1.10×10^4 (0.94)	3.22×10^5 (16.89)
LWP (g m^{-2})	0.69 (1.02)	0.66 (0.77)	$-1.86 (-2.32)$	4.57 (5.10)
IWP (g m^{-2})	0.05 (0.37)	0.10 (0.99)	0.42 (3.69)	0.13 (1.48)
SWCF (W m^{-2})	$-0.41 (0.86)$	$-0.63 (1.17)$	0.400 (-1.48)	$-2.87 (3.47)$
LWCF (W m^{-2})	0.08 (0.35)	0.031 (0.15)	0.13 (0.57)	0.11 (0.52)
CLDTOT (%)	0.12 (0.17)	0.17 (0.22)	0.011 (0.014)	1.05 (1.45)
CLDHGH (%)	0.016 (0.039)	$-0.0082 (-0.021)$	$-0.027 (-0.071)$	$-0.18 (-0.47)$
CLDMED (%)	0.078 (0.26)	0.19 (0.55)	0.20 (0.54)	0.017 (0.054)
CLDLOW (%)	0.13 (0.33)	0.14 (0.24)	$-0.43 (-0.69)$	1.35 (2.52)
PRECT (mm day^{-1})	$-0.0011 (-0.038)$	0.0042 (0.17)	0.019 (0.71)	0.040 (1.66)

9
 10
 11



12
13
14
15
16
17
18

Table 7. CCN and INP effects of MOA on SWCF, and the values in the table are the mean change and relative change (%). The CCN effect is calculated between CTL and B14_D15 experiments, and the INP effect is calculated between B14_D15 and B14D15_M18 experiments, with the bold font indicated the maximum change.

	ANN	MAM	JJA	SON	DJF
20–90S CCN	-0.84 (1.58)	-0.47 (1.16)	0.48 (-1.78)	-0.59 (0.95)	-2.78 (3.36)
INP	0.22 (-0.50)	0.084 (-0.20)	-0.080 (0.30)	0.94 (-1.51)	-0.088 (0.10)
global CCN	-0.41 (0.85)	-0.21 (0.48)	-0.43 (0.89)	0.027 (-0.056)	-1.01 (1.96)
INP	-0.0037 (0.0077)	0.047 (-0.11)	0.27 (-0.54)	-0.16 (0.33)	-0.17 (0.33)

19
20



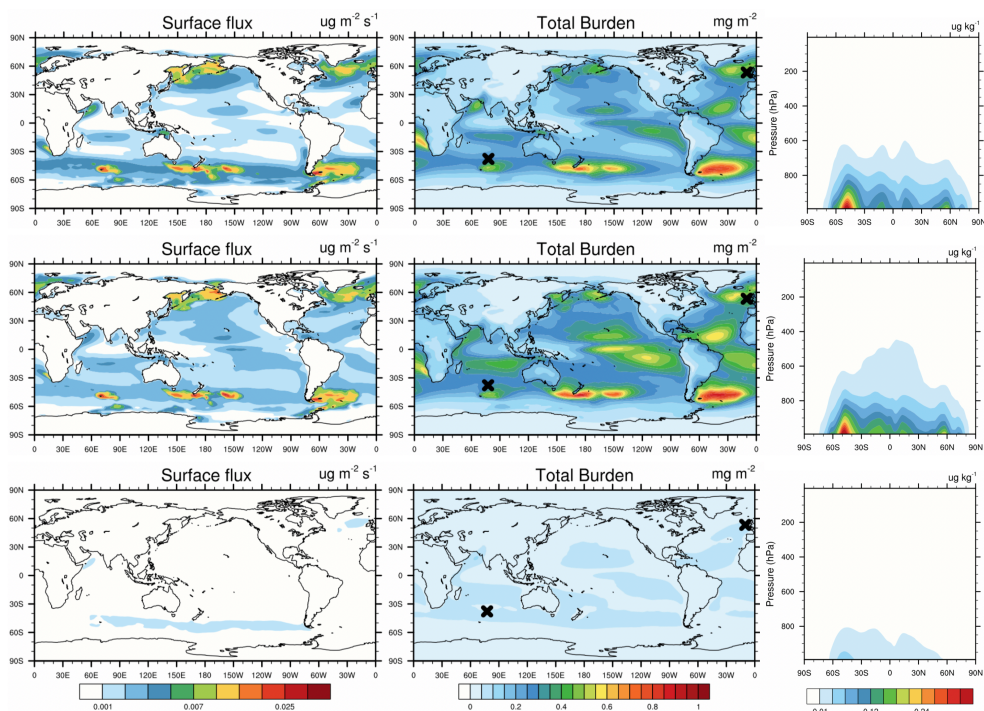
21 Table 8. CCN and INP effect of MOA on LWCF, and the values in the table are the mean change and
22 relative change (%). The CCN effect is calculated between CTL and B14_D15 experiments, and the INP
23 effect is calculated between B14_D15 and B14D15_M18 experiments, with the bold font indicated the
24 maximum change.
25

	ANN	MAM	JJA	SON	DJF
20–90S CCN	0.064 (0.30)	0.033 (0.15)	−0.21 (−0.93)	0.29 (1.39)	0.15 (0.73)
INP	−0.033 (−0.15)	−0.15 (−0.68)	0.35 (1.5)	−0.29 (−1.35)	−0.042 (−0.20)
global CCN	0.064 (0.27)	−0.0097 (−0.040)	−0.032 (−0.13)	0.0890 (0.38)	0.21 (0.91)
INP	0.020 (0.085)	−0.12 (−0.50)	0.21 (0.85)	0.035 (0.15)	−0.039 (−0.17)

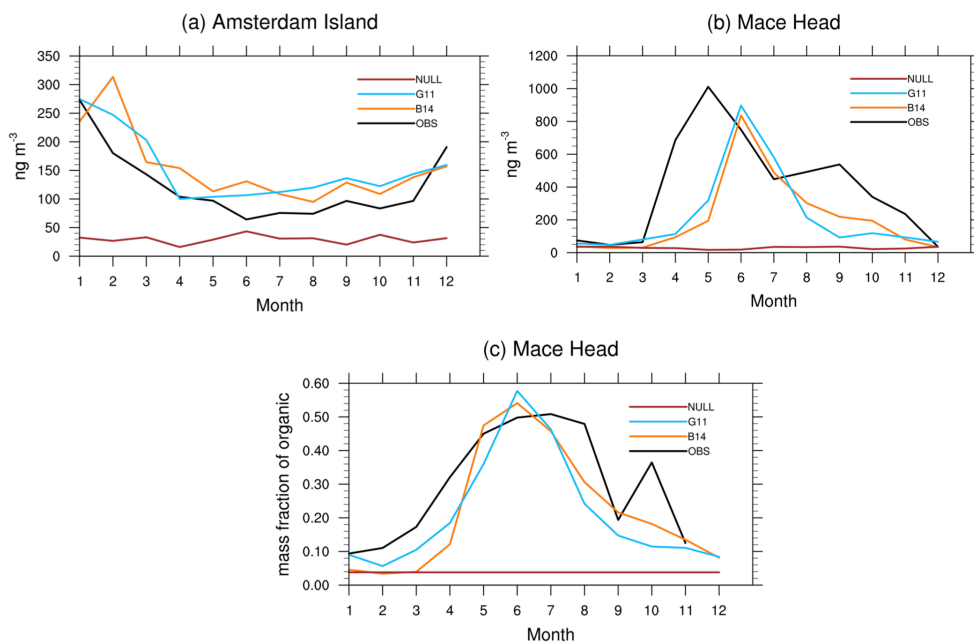
26
27
28



29 **Figures**
30



31
32 Figure 1. Spatial distributions of annual mean surface flux (first column, in unit of $\mu\text{g m}^{-2} \text{s}^{-1}$) and
33 vertically-integrated (column) burden of MOA (second column, in unit of mg m^{-2}), and latitude-pressure
34 cross-sections of annual mean MOA mixing ratio (third column, in unit of $\mu\text{g kg}^{-1}$) from the B14 (first row),
35 G11 (second row), and NULL (third row) experiments. The right black cross in the second row indicates
36 the position of Mace Head, and the left black cross indicates the position of Amsterdam Island.
37
38

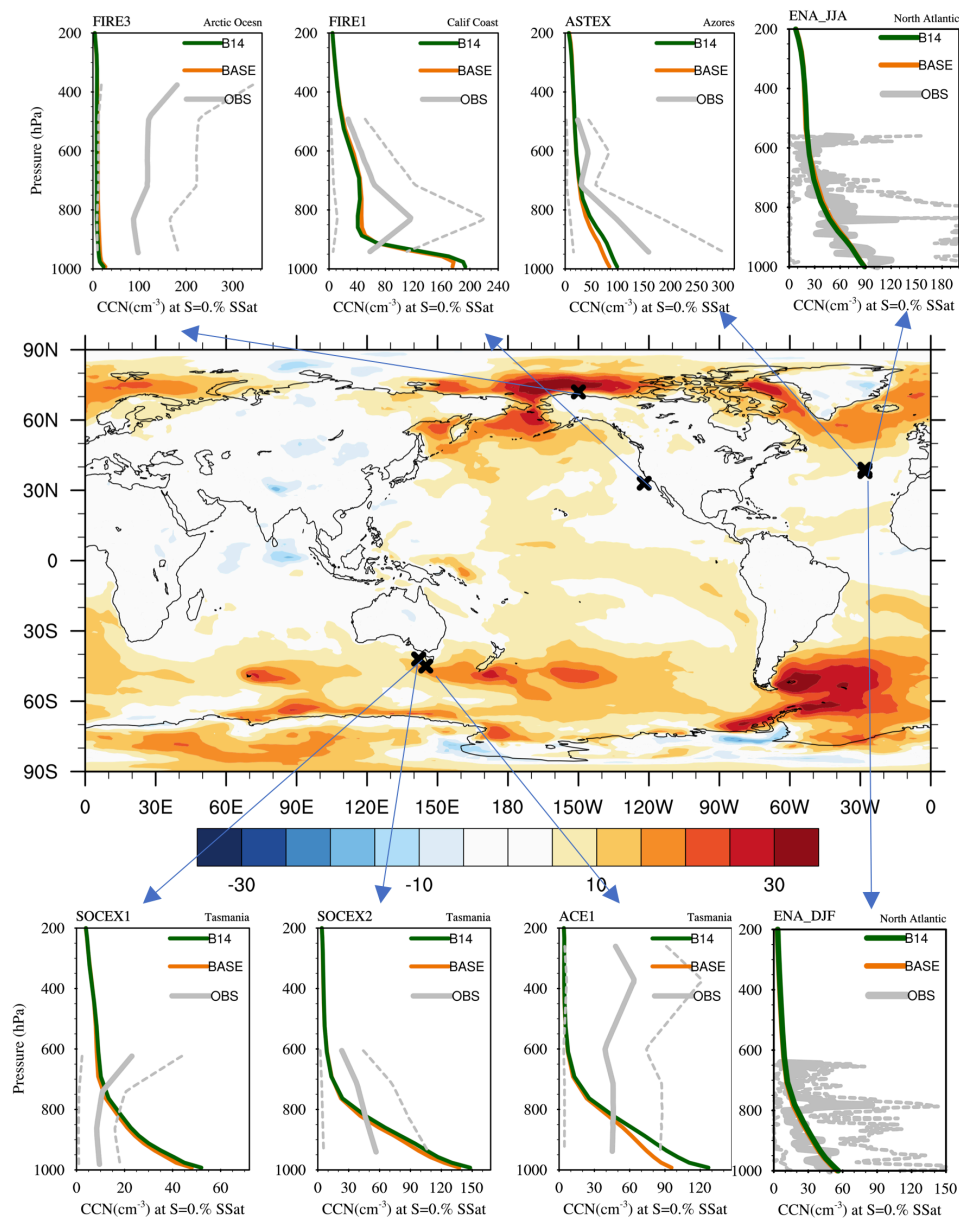


39
40
41
42
43
44
45

Figure 2. Monthly averaged concentrations of MOA at (a) Amsterdam Island and (b) Mace Head Ireland; and (c) monthly averaged mass fraction of MOA in SSA at Mace Head Ireland. The locations of Amsterdam Island and Mace Head Ireland are shown in Figure 1.



46

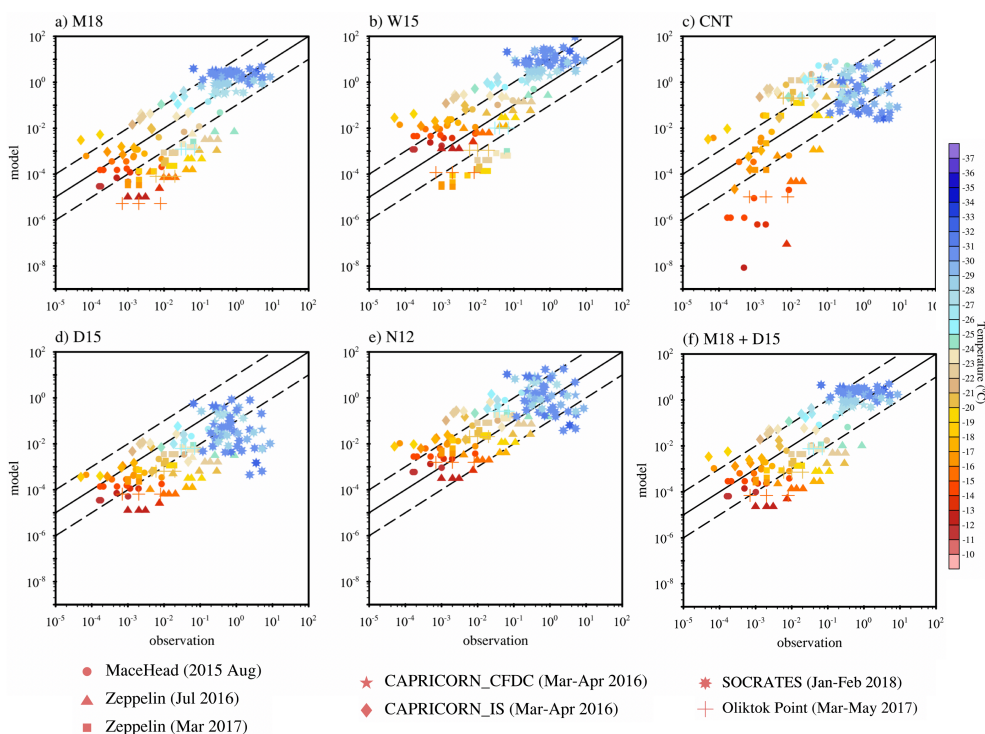


47
 48
 49
 50
 51
 52
 53
 54
 55

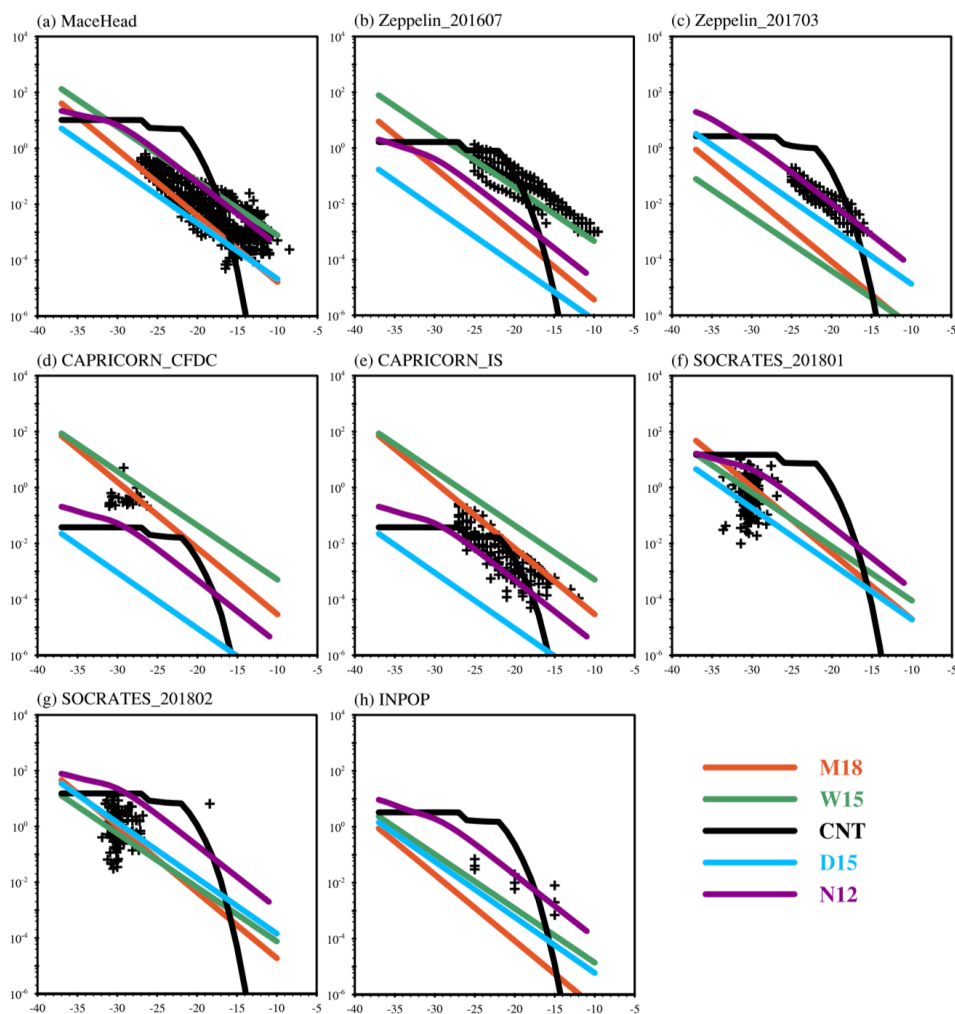
Figure 3. Spatial distribution of annual mean percentage changes of surface CCN concentrations at 0.1% supersaturation due to MOA, and vertical distribution of CCN concentrations at 0.1% supersaturation from eight measurements (solid gray lines), BASE (solid orange line) and B14_D15 (solid green line). Dashed lines outline a range of 10th and 90th percentiles for measurements in different field campaigns: FIRE1 (the First International Satellite Cloud Climatology Project Reginal Experiment) locates at 33° N and 238° W in California coast, the data is collected during June to July, 1987; the FIRE3 locates at 72° N and 210° W in Arctic Ocean, the data is collected during May, 1998; the ASTEX (Atlantic Stratocumulus



56 Transition Experiment) locates at 38° N and 332° W in Azores, the data is collected during June, 1992; the
57 SOCEX1 (Southern Ocean Cloud Experiment) is located as -42° S and 142° E in Tasmania, the data is
58 collected during July 1993; the data of SOCEX2 is collected during January to February 1995; the ACE1
59 (Aerosol Characterization Experiment) locates at -45° S , 145° E in Tasmania, the data is collected during
60 November to December, 1995; and the ENA_JJA(Eastern North Atlantic) locates at 39° N and 332° W in
61 Eastern North Atlantic, the data is collected during June to August, while ENA_DJF is collected during
62 December, January, and February, 2006 to 2020.
63

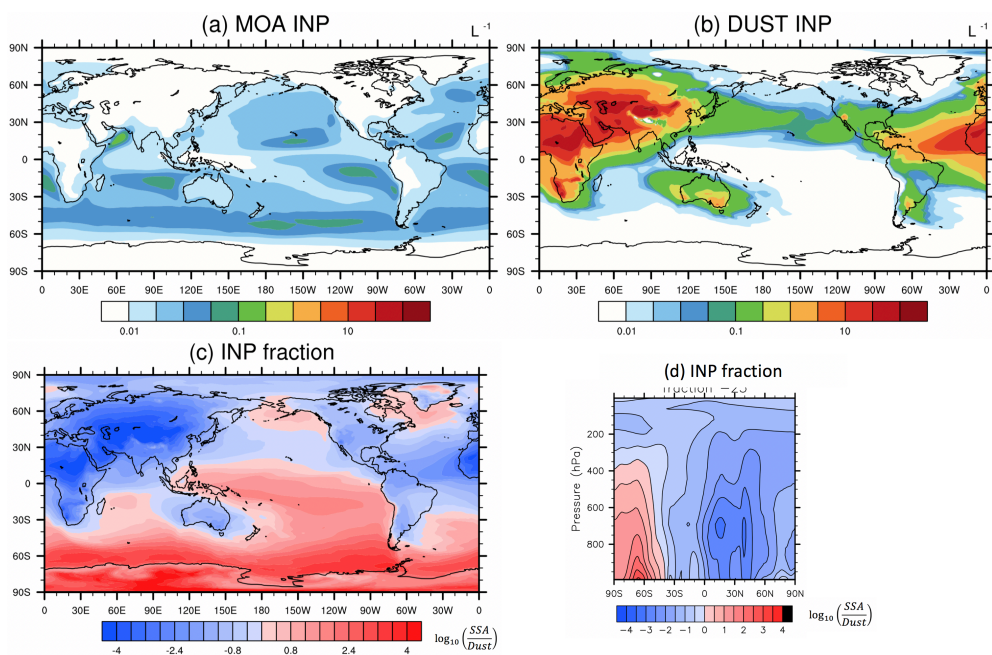


64
 65 Figure 4. Comparison of simulated vs. observed INP number concentrations for different simulations:
 66 (a) MOA INPs from M18 [McCluskey et al., 2018], (b) MOA INPs from W15 [Wilson et al., 2015],
 67 (c) dust INPs from CNT [Wang et al., 2014], (d) dust INPs from D15 [DeMott et al., 2015], (e) dust
 68 INPs from N12 [Niemand et al., 2012], and (f) sum of dust and MOA INPs from D15 and M18.
 69 Dashed lines outline a factor of 10 about the 1:1 line (solid) in all the panels. Color bar shows the
 70 observed temperature in °C, while different markers represent different field campaigns. Zeppelin site
 71 locates at 78.9081° N, 11.8814° E, 475 m above mean sea level in NyÅlesund, Svalbard, the INP data is
 72 collected during July 2016 and March 2017 [Tobo et al., 2019]; Oliktok Point site locates at 70.50° N
 73 149.89°W, the INP data is collected during March-May 2017 [Creamean et al., 2018]; CAPRICORN
 74 (Clouds, Aerosols, Precipitation, Radiation, and Atmospheric Composition over the Southern Ocean) INP
 75 data is collected on ships during 13 March to 15 April in 2016 over the Southern Ocean [McCluskey, Hill,
 76 Humphries, et al., 2018a]; Mace Head site locates at 53.32°N, 9.90°W, the INP data is collected during
 77 August 2015 [McCluskey, Ovadnevaite, Rinaldi, et al., 2018b]; SOCRATES (Southern Ocean Clouds,
 78 Radiation, Aerosol Transport Experimental Study) INP data is collected on flights during January-February
 79 2018 over the Southern Ocean by Paul DeMott (https://data.eol.ucar.edu/master_lists/generated/socrates/).
 80



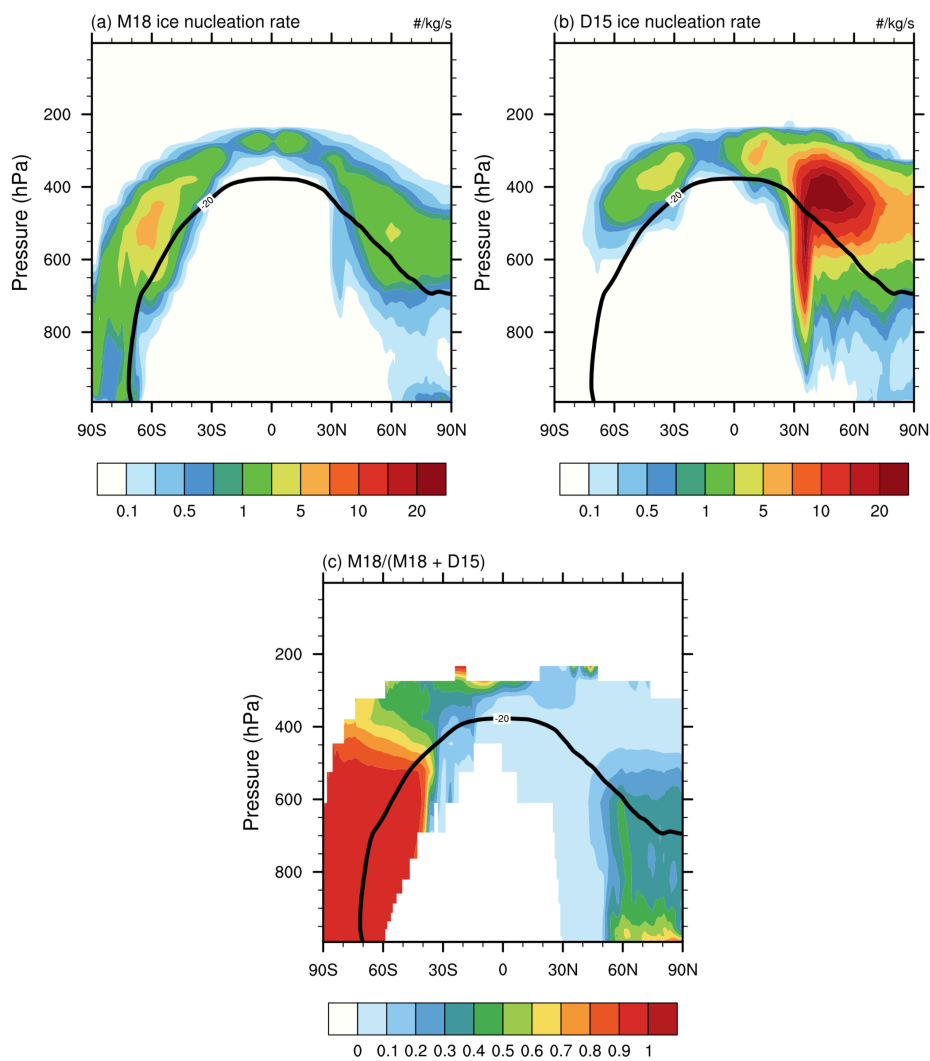
81
82
83
84
85
86
87

Figure 5. Modeled and observed INP concentrations as a function of temperature. The black crosses indicate INP measurements, and lines show model results from different parameterizations (Table 4). Model grid points are selected at the same pressure levels and longitudes and latitudes as field measurements.

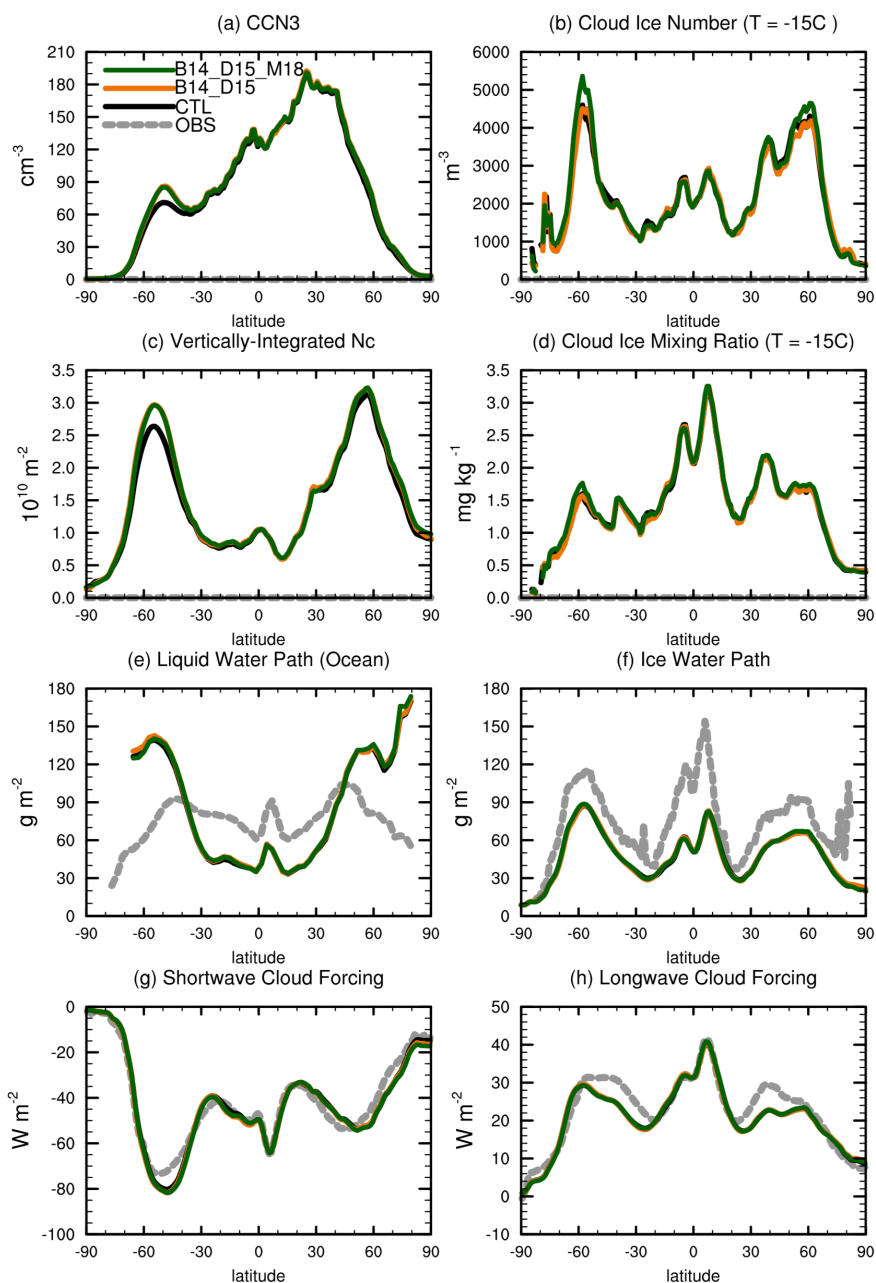


88
89
90
91
92
93

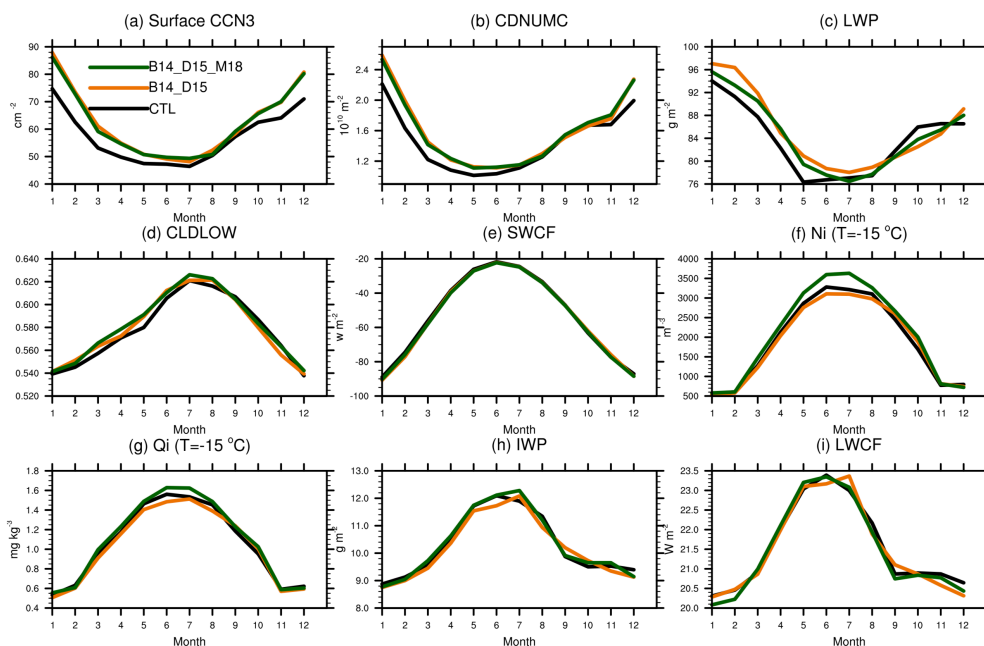
Figure 6. Spatial distribution of annual mean concentrations of (a) MOA INPs, (b) dust INPs, and (c) ratio of MOA INP concentration to dust INP concentration at 950 hPa, and (d) vertical cross sections of ratio of MOA INP concentration to dust INP concentration. INP concentrations are diagnosed at temperature of -25°C .



94
95 Figure 7. Annual zonal mean pressure-latitude cross sections of ice nucleation rates from (a) MOA, (b) dust,
96 and (c) MOA fraction of total ice production rate.
97



98
99
100
101
102
103
104
Figure 8. Annual zonal-mean distributions of (a) surface CCN concentration at $S=0.1\%$, (b) cloud ice number concentration on $T=-15^{\circ}\text{C}$ isotherm, (c) vertically-integrated cloud droplet number concentration, (d) cloud ice mass mixing ratio on $T=-15^{\circ}\text{C}$ isotherm, (e) liquid water path over ocean, (f) ice water path, (g) shortwave cloud forcing, and (h) longwave cloud forcing for CTL (black), B14_D15 (orange), and B14_D15_M18 (green), along with available observations (gray dashed lines) as references.



105
106
107
108
109
110

Figure 9. Seasonal cycle of (a) surface CCN at 0.1% supersaturation, (b) vertically-integrated cloud droplet number concentration, (c) liquid water path, (d) low cloud amount, (e) shortwave cloud forcing, (f) cloud ice number concentration on $T=-15^{\circ}\text{C}$ isotherm, (g) cloud ice mass mixing ratio on $T=-15^{\circ}\text{C}$ isotherm, (h) ice water path (IWP), and (i) LWCF, for CTL (black), B14_D15 (orange) and B14_D15_M18 (green).